Convective heat transfer in the thin film of an elongated bubble in the absence of phase change

Paolo Botticini, Davide Picchi,* and Pietro Poesio
Department of Mechanical and Industrial Engineering, Università degli Studi di Brescia, Brescia 25123, Italy

(Received 28 January 2026; accepted 12 May 2026; published 3 June 2026)

The injection of an elongated bubble into a microchannel is a well-established strategy for enhancing convective heat transfer, with applications ranging from electronics cooling to miniaturized heat exchangers. So far, a rigorous characterization of the heat removal capabilities of elongated bubbles (also known as Bretherton's or Taylor's bubbles) is still lacking. To address this gap, we investigate the forced convection problem in the thin film formed by an elongated bubble under uniform wall heat flux, examining the competition between advection, diffusion, viscous dissipation, and an imposed heat flux at the channel walls. By means of two-scale asymptotic analysis, we derive a one-dimensional advection-diffusion–heat-transfer equation with shape-dependent effective coefficients. This model generalizes the classical Graetz problem to capillary-driven flows and extends the Aris-Taylor dispersion to the case of an elongated bubble, clarifying the interplay between the imposed heat flux and the recirculating flow patterns at both front and rear menisci. Interestingly, the model recovers the Péclet-squared scaling of the effective diffusion coefficient and can be used to determine the heat transfer coefficient in the film region. In fact, we derive a closed-form scaling law for the Nusselt number, revealing the influence of the problem parameters (i.e., the bubble profile and the axial temperature gradient) and the dimensionless groups (Péclet, Brinkman, and capillary numbers) on forced convection. Grounded in first principles, our analysis contributes to a deeper understanding of capillary-driven forced convection in confined environments.

DOI: 10.1103/tf8n-pmmb

I. INTRODUCTION

Understanding the dynamics of two-phase gas-liquid flows in microchannels is relevant to many engineering application, ranging from heat-exchangers to small-scale reactors. In these contexts, the topology of the flowing phases determines the existence of several flow patterns (i.e., stratified, core-annular, intermittent or slug, and dispersed flows) that profoundly affect the heat transfer rate. In particular, due to the dominant effect of surface tension, the most common flow pattern is characterized by the presence of elongated bubbles surrounded by a thin liquid film and separated by liquid plugs (see, for example, Ref. [1]). When a long bubble flows in a capillary tube, in fact, it assumes the typical bullet shape and is often referred to as a Taylor or Bretherton bubble after their seminal works in the early 1960s [2,3]. Historically, the name "Taylor bubble" was proposed for the first time by Griffith and Wallis [4] and Brown [5], referring to large gas volumes rising in a large-diameter tube after the work of Davies and Taylor [6], but, later on, it has also been used to denote trains of elongated bubbles in small-diameter tubes (see Taylor flow in Refs. [7,8]).

So far, most of the studies have focused on heat transfer enhancement closed to an elongated bubble in the context of boiling and cooling applications such as in the context of heat-pipes [9,10].

*Contact author: davide.picchi@unibs.it

These results are summarized in recent review papers (just to mention a few [11–13]) where the evaporating/condensing elongated bubble is often investigated experimentally [14,15], or in terms of mechanistic models, such as the widely used three-zone model developed by Thome *et al.* [16], Dupont *et al.* [17], Szczukiewicz *et al.* [18], or by means of numerical simulations [19,20]. Also, there is a growing interest in the dynamics of evaporation in very thin films, known as microlayer [21–24].

However, the heat transfer problem in the absence of phase change, where the elongated bubbles are obtained by injection of an immiscible dispersed phase, has received limited attention. Although this class of two-phase flows finds application in compact heat exchangers embedded in printed circuit boards [25,26] and microreactors [1], most of the existing works is primarily experimental or numerical (see the recent reviews in Refs. [26–29]). A theoretical framework, able to provide a better understanding of the relevant physical mechanisms at play in forced convection around a non evaporating/condensing elongated bubble, is still lacking. Specifically, experimental evidences point out that the presence of elongated bubbles enhances heat transfer compared to single-phase flow but the impact of flow characteristics (e.g., the velocity field, the slug length, the liquid fraction, fluid thermal properties, and thermal boundary conditions) on thermal performance [30] is still not fully understood.

In fact, it is common practice to model the heat transfer coefficient using semiempirical correlations (e.g., Refs. [31–35]) formulating the Nusselt number in analogy with the single-phase scenario [36,37]. Unfortunately, the predictions of these correlations presents a large variability [26]. Only recently, Che *et al.* [38] proposed a model for a train of elongated bubbles, but, since the bubbles are treated as a sequence of rectangular wall-wetting plugs, the effect of the the thin film surrounding the bubble on forced convection is not accounted for.

One way to deal with this thermal problem is to take inspiration from hydrodynamic dispersion, which has been extensively investigated from a theoretical perspective, starting from the pioneering works of Taylor [39] and Aris [40], later extended to various contexts (e.g., Refs. [41–44]) including Taylor bubbles [45]. In fact, heat and mass transfer share similar governing equations, while the boundary conditions reflect different physical constraints across interfaces (i.e., a solid wall or other phases). In particular, the constant heat flux boundary condition and viscous dissipation term are formally analogous to a permeable boundary and a volumetric chemical reaction source in mass transfer, respectively. However, the mass transfer problem considered by Picchi and Poesio [45] is based on a Robin boundary condition, which models a finite-rate interfacial exchange process (e.g., absorption, desorption, dissolution, evaporation, or noninstantaneous surface reactions). In contrast, the isoflux condition adopted here corresponds to the limiting case of an infinitely large transfer coefficient (i.e., vanishing interfacial resistance), which leads to a different coupling between the solid and fluid phases and, consequently, to a distinct transport behavior. So far, extensions of dispersion theory to heat transfer remain limited, mostly restricted to single-phase flows in insulated or radiant pipes [46,47] and combustion processes [48]. In the context of two-phase flows, an effective model for two-phase forced convection valid for both gas-liquid and liquid-liquid core-annular flows was developed in Botticini *et al.* [49]. Although the core-annular pattern has proven to be a useful idealization of more complex flow regimes such as elongated bubbles (see Refs. [16,50–52]), a rigorous analytical description of heat transfer in the thin film around a single elongated bubble is still lacking.

To address these limitations, the goal of this paper is to investigate the forced convection around a single elongated bubble in a horizontal capillary tube under uniform wall heat flux. We will focus on regimes where phase change is absent and inertial and gravitational effects are negligible. Starting from first principles, we generalize the perturbation scheme that characterizes the classical Taylor dispersion to the temperature field in the thin-film flow surrounding an elongated inviscid bubble. Specifically, the flow field and the shape of the bubble are the ones proposed by Bretherton [3] (i.e., the low capillary number regime), as typical of a broader class of coating problems [53,54]. We aim to obtain a reduced-order effective description that explains the physical mechanisms behind the enhancement on the heat transfer coefficient.

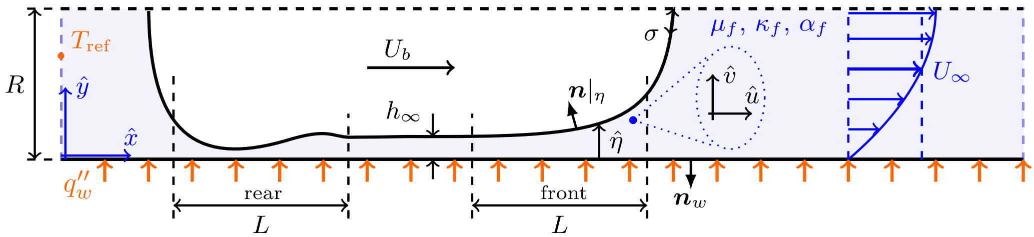

FIG. 1. Sketch of the elongated bubble moving in a uniformly heated channel. The hat operator denotes the dimensional variables.

The manuscript is structured as follows. We first review the thin–film flow around the elongated bubble (Sec. II A), present its energy balance (Sec. II B) and make the problem dimensionless (Sec. II C). By means of two-scale asymptotic expansion (Sec. III A), we derive a one-dimensional upscaled equation for the depth-averaged film temperature as function of space and time (Sec. III B), and specify its applicability conditions (Sec. III C). The resulting effective model is then solved numerically (Sec. III D) to study the evolution of the effective heat-transfer coefficients and the temperature field (Sec. IV A). Subsequently, we derive a closed-form expression for the local Nusselt number (Sec. IV B), quantifying the competition between convection and conduction in the liquid film. Finally, we analyze the heat transfer dynamics thorough the film in terms of the averaged Nusselt number (Sec. IV C). A summary discussion is presented in the concluding section (Sec. V).

II. PROBLEM FORMULATION

A. Flow in the thin film of the elongated bubble

We consider a single inviscid elongated bubble that flows at speed U_b in an infinitely long channel of half-size R, see Fig. 1, in regimes where inertia and gravity can be neglected, namely, the Reynolds and the Bond number are both small (i.e., $\mathrm{Re} = \rho_f\, U_b\, R/\mu_f \ll 1$ and $\mathrm{Bo} = \rho_f\, g R^2/\sigma \ll 1$ where ρ_f, μ_f, and σ are the fluid density, viscosity, and surface tension, respectively). The motion is driven by a steady flow far behind the bubble with average speed U_∞ and the bubble is assumed to be sufficiently long so that there exists a region of uniform film thickness $h_\infty \ll R$ at the bubble center.

At the front and the rear of the bubble the meniscus is spherical, while, in the transition region in between, it follows the similarity profile typical of the Landau-Levich-Derjaguin-Bretherton problem [3,54]. Specifically, in a reference frame attached to the bubble, the film thickness $\hat{\eta}(\hat{\xi},\, \hat{t}) = \hat{\eta}(\hat{x} - U_b \hat{t},\, \hat{t})$ is described by the following similarity equation [3]

$$\frac{\mathrm{d}^3\eta}{\mathrm{d}\xi^3} = \frac{\eta - 1}{\eta^3}, \tag{1}$$

with

$$\xi = \frac{\hat{\xi}}{h_\infty (3\,\mathrm{Ca})^{-1/3}}, \qquad \eta = \frac{\hat{\eta}}{h_\infty}, \qquad \text{and} \qquad \mathrm{Ca} = \frac{\mu_f\, U_b}{\sigma} \ll 1, \tag{2}$$

where ξ is is the dimensionless stretched axial coordinate, η is the dimensionless film thickness, and Ca is the capillary number. The Bretherton's similarity equation results from the lubrication theory and holds in the transition region of length L depicted in Fig. 1, whose order of magnitude is obtained balancing the pressure drop along the axial direction with the pressure jump generated by the curved meniscus as $L = h_\infty (3\,\mathrm{Ca})^{-1/3}$; see Refs. [3,54,55].

The bubble meniscus is obtained by integration of (1) starting from the uniform film where $\eta \approx 1$. Specifically, integrating Eq. (1) in the positive direction gives the front profile, which, for $\eta \gg 1$, joins a parabolic profile of constant curvature. There, the meniscus is matched to a spherical cap of radius R, giving the asymptotic relation for the film thickness,

$$\frac{h_\infty}{R} = 0.643\,(3\,\mathrm{Ca})^{2/3}. \tag{3}$$

Integration of Eq. (1) toward the negative direction yields the rear profile, which exhibits the typical undulations; see Fig. 9. The integration in both the front and the rear is carried out numerically following the methodology outlined in Bretherton [3], Picchi *et al.* [55]. The Bretherton equation (1) together with the asymptotic matching condition (3) is accurate at sufficiently small capillary numbers (e.g., Habibi Matin and Moghaddam [56] reports $\mathrm{Ca} < 0.003$), such that the liquid–vapor interface in the transition region is nearly parallel to the channel wall ($|\partial_{\hat{\xi}}\hat{\eta}| \ll 1$), and the liquid film thickness is much smaller than the channel radius ($\hat{\eta} \ll R$). Deviations from Bretherton's theory when these assumptions break down are discussed in Appendix A.

Note that, although Bretherton theory [3] builds on a planar geometry, in the small capillary number limit ($\mathrm{Ca} \ll 1$) the circular and planar geometries are asymptotically equivalent, as shown in Appendix B. Interestingly, the elongated bubble always flows faster compared to the flow ahead, and mass conservation yields [54]

$$\frac{U_b - U_\infty}{U_b} = (1+m)\,\frac{h_\infty}{R}, \quad \text{where} \quad m = \begin{cases} 0 & \text{for planar channel,} \\ 1 & \text{for circular tube.} \end{cases} \tag{4}$$

B. Energy balance in the film

We study the forced convection in the thin liquid film around the elongated bubble subjected to a constant wall heat flux q''_w in the absence of phase change, as shown in Fig. 1. The internal energy balance in a reference frame attached to the bubble is given by

$$\rho_f\, c_p\left(\frac{\partial \hat{T}}{\partial \hat{t}} + (\hat{u} - U_b)\,\frac{\partial \hat{T}}{\partial \hat{\xi}} + \hat{v}\,\frac{\partial \hat{T}}{\partial \hat{y}}\right) = \kappa_f\left(\frac{\partial^2 \hat{T}}{\partial \hat{\xi}^2} + \frac{\partial^2 \hat{T}}{\partial \hat{y}^2}\right) + \hat{\Phi}, \tag{5}$$

where $\hat{T}(\hat{\xi}, \hat{y}, \hat{t})$, c_p, κ_f are the fluid temperature, the isobaric mass heat capacity, and the thermal conductivity of the liquid, respectively, and $\hat{u}(\hat{\xi}, \hat{y})$ and $\hat{v}(\hat{\xi}, \hat{y})$ are the velocity profiles in the axial and traverse direction obtained via the lubrication approximation as in Ref. [3]; the thermal diffusivity is defined as $\alpha_f = \kappa_f/(\rho_f\, c_p)$. All the physical properties are assumed uniform and constant. The term $\hat{\Phi}$ is the rate of viscous dissipation of mechanical energy per unit mass and reads

$$\hat{\Phi} = \mu_f\left[2\left(\frac{\partial \hat{u}}{\partial \hat{\xi}}\right)^2 + 2\left(\frac{\partial \hat{v}}{\partial \hat{y}}\right)^2 + \left(\frac{\partial \hat{u}}{\partial \hat{y}} + \frac{\partial \hat{v}}{\partial \hat{\xi}}\right)^2\right]. \tag{6}$$

At the channel wall, $\hat{y} = 0$, we assume that a uniform heat flux is imposed [57], leading to

$$q''_w = -\kappa_f(\hat{\nabla}\hat{T}\cdot \boldsymbol{n}_w)|_{\hat{y}=0} = \kappa_f\,\frac{\partial \hat{T}}{\partial \hat{y}}\bigg|_{\hat{y}=0}, \tag{7}$$

where the outward-directed unit vector is given by $\boldsymbol{n}_w = (0; -1)$, as shown in Fig. 1. At the film-bubble interface, $\hat{y} = \hat{\eta}$, we impose continuity of temperature and heat flux, while the entire domain is initialized with a temperature equal to T_{ref}.

C. Dimensionless formulation

To make the problem dimensionless, we identify its characteristic scales. Specifically, the relevant scale in the transverse direction is the uniform film thickness h_∞ while in the axial direction we use the length of the transition region L. This allow us to define a small-scale parameter as

$$\varepsilon = \frac{h_\infty}{L} = (3\,\mathrm{Ca})^{1/3} \ll 1. \tag{8}$$

Among the different timescales of the thermal problem, namely, the transversal, $\mathcal{T}_{d,h} = h_\infty^2/\alpha_f$, and longitudinal, $\mathcal{T}_{d,L} = L^2/\alpha_f$, heat diffusion timescales, and the advective timescale, $\mathcal{T}_a = L/U_b$, the time in the energy balance is made dimensionless according to the advective one by analogy with the Aris-Taylor dispersion [39,40]. This means that we are interested in modeling a time window where traverse diffusion can be considered instantaneous, but longitudinal diffusion competes with advection.

Thus, we make the energy balance and its boundary conditions dimensionless by introducing the following dimensionless quantities:

$$\vartheta = \frac{\rho_f\, c_p\,(\hat{T} - T_{\mathrm{ref}})\, U_b\, h_\infty}{|q_w''| L}, \quad t = \frac{\hat{t}}{L/U_b}, \quad u = \frac{\hat{u}}{U_b}, \quad v = \frac{\hat{v}}{\varepsilon\, U_b}, \quad \Phi = \frac{\hat{\Phi}}{\mu_f\, U_b^2/h_\infty^2}. \tag{9}$$

The dimensionless temperature ϑ quantifies the energy convected within the film relative to that supplied through the wall, with the temperature deviation $\hat{T} - T_{\mathrm{ref}}$ serving as the main variable [58]. The axial and transverse coordinates are made dimensionless based on L and h_∞, respectively, according to the Bretherton theory, i.e., $\xi = \hat{\xi}/L$ and $y = \hat{y}/h_\infty$; see Eq. (2). This leads to

$$\varepsilon^2\,\mathrm{Pe}\left[\frac{\partial\vartheta}{\partial t} + (u-1)\frac{\partial\vartheta}{\partial\xi} + v\,\frac{\partial\vartheta}{\partial y}\right] = \varepsilon^2\,\frac{\partial^2\vartheta}{\partial\xi^2} + \frac{\partial^2\vartheta}{\partial y^2} + \varepsilon^2\,\mathrm{Pe}\,\mathrm{Br}\,\Phi, \tag{10}$$

where $y \in [0;\, \eta(\xi)]$ and the absolute components $(u,\, v)$ of the velocity field and the viscous dissipation function $\Phi(\eta,\, y)$ are given in Appendix C. The Péclet number can be seen as the ratio between advection and thermal diffusion and is defined as

$$\mathrm{Pe} = \frac{L\,U_b}{\alpha_f}. \tag{11}$$

When $\mathrm{Pe} \ll 1$, diffusion dominates over advection, while for $\mathrm{Pe} \gg 1$, advection plays a major role with respect to diffusion. The Brinkman number accounts for the competition between the thermal power per unit mass produced by viscous dissipation and the one transferred from the solid walls, and is defined as

$$\mathrm{Br} = \frac{\mu_f\, U_b^2}{|q_w''|\, h_\infty}. \tag{12}$$

The uniform flux boundary condition imposed at the wall, $y = 0$, leads to

$$\left.\frac{\partial\vartheta}{\partial y}\right|_{y=0} = \nu\,\varepsilon^2\,\mathrm{Pe}, \quad \text{with} \quad \nu = \mathrm{sgn}(q_w''), \tag{13}$$

where $\nu = \pm 1$ denotes heat flux leaving or entering the tube, respectively. Typically, $\nu = -1$ in experimental setups where the tube is heated via external resistive elements (e.g., Ref. [59]). At the gas-liquid interface, $y = \eta$, the outward unit normal vector to the liquid phase (see Fig. 1) is

$$\boldsymbol{n}|_{y=\eta} = (n_\xi;\, n_y) = \left(\frac{-\varepsilon\,\mathrm{d}\eta/\mathrm{d}\xi}{\sqrt{1+\varepsilon^2\,(\mathrm{d}\eta/\mathrm{d}\xi)^2}};\, \frac{1}{\sqrt{1+\varepsilon^2\,(\mathrm{d}\eta/\mathrm{d}\xi)^2}}\right), \tag{14}$$

and the continuity of thermal fluxes, $\kappa_f(\hat{\boldsymbol{\nabla}}\hat{T}_f \cdot \boldsymbol{n})|_{\hat{y}=\hat{\eta}} = \kappa_b(\hat{\boldsymbol{\nabla}}\hat{T}_{\mathrm{gas}} \cdot \boldsymbol{n})|_{\hat{y}=\hat{\eta}}$, yields

$$\left.\left(\frac{\partial\vartheta}{\partial y} - \mathcal{K}\,\frac{\partial\vartheta_{\mathrm{gas}}}{\partial y}\right)\right|_{y=\eta} - \varepsilon^2\,\frac{\mathrm{d}\eta}{\mathrm{d}\xi}\left.\left(\frac{\partial\vartheta}{\partial\xi} - \mathcal{K}\,\frac{\partial\vartheta_{\mathrm{gas}}}{\partial\xi}\right)\right|_{y=\eta} = 0, \tag{15}$$

where the dimensionless bubble temperature is defined as $\vartheta_{\text{gas}} = \rho_f\, c_p\, (\hat{T}_{\text{gas}} - T_{\text{ref}})\, U_b\, h_\infty/(|q''_w|L)$, and

$$\mathcal{K} = \frac{\kappa_b}{\kappa_f} \tag{16}$$

is the conductivity ratio. In this work, we are primarily interested in gas-liquid systems, where such ratio is typically of $\mathcal{O}(\mathcal{K}) = 10^{-2}$; see Table I in Botticini *et al.* [49]. We will show in the following that, when $\mathcal{K} \to 0$, the phases are thermally decoupled, reducing the boundary condition (15) to a one-sided model, and making the temperature continuity condition at the interface, namely, $\vartheta|_{y=\eta} = \vartheta_{\text{gas}}|_{y=\eta}$, unimportant for the purpose of our analysis. The problem is closed imposing the initial condition as a uniform temperature distribution for both phases in the absolute reference frame $(x,\ y,\ t)$:

$$\vartheta(0,\ y,\ 0) = \vartheta_{\text{gas}}(0,\ y,\ 0) = 0, \tag{17}$$

and its reformulation in the moving reference frame $(\xi,\ y,\ t)$ will be discussed in Sec. III D.

III. THEORETICAL DERIVATION

In this section we derive the one-dimensional advection-diffusion-heat-transfer equation that describes the forced convection in the film region of an elongated bubble. First we outline the mathematical procedure, and then we apply it to the energy equation in the thin film.

A. Two-scale asymptotics of the energy equation

The main idea is to obtain a reduced-order model for the forced convection in the thin film in terms of its averaged temperature. To do so, we use two-scale asymptotic expansions of the energy equation building on the work of Ref. [60]:

(1) We start from the energy balance in dimensionless formulation, Eqs. (10), (13), and (15), where a small-scale parameter $\varepsilon \ll 1$ has been identified to decouple axial and transverse heat transfer.

(2) Each dimensionless group in the governing equations (11), (12), and (16) is expressed in terms of integer powers of the scale parameter [or the capillary number, see Eq. (2)]:

$$\text{Pe} = \varepsilon^{-p}, \quad \text{Br} = \varepsilon^{b}, \quad \mathcal{K} = \varepsilon^{k}, \tag{18}$$

where the exponents p, b, and k define the system behavior and can be selected independently. This is typical of perturbation methods (see, e.g., Refs. [61,62]) and allows the different terms of the expanded energy balance to jump from one order to the other controlled by the order of magnitude of the dimensionless numbers.

(3) The temperature $\vartheta(\xi,\ y,\ t)$ is, then, expanded in Eqs. (10), (13), and (15) into a power series as

$$\vartheta(\xi,\ y,\ t) = \vartheta^{(0)}(\xi,\ y,\ t) + \varepsilon^{2-p}\,\vartheta^{(1)}(\xi,\ y,\ t) + \varepsilon^{2(2-p)}\,\vartheta^{(2)}(\xi,\ y,\ t) + \cdots, \tag{19}$$

where the perturbation parameter is the ratio of the competing characteristic timescales of thermal dispersion, i.e., $\mathcal{T}_{d,h}/\mathcal{T}_a = \varepsilon^{2-p}$. This choice helps in identifying the desired time window where the transverse diffusion can be considered instantaneous if compared to axial diffusion and advection.

(4) Substituting the power-series expansion (19) into the governing equations and collecting terms by order yields a cascade of boundary-value problems for $\vartheta^{(n)}$ that are solved sequentially. The goal is to find an equation for the averaged temperature in the film defined as

$$\langle\vartheta\rangle \equiv \frac{1}{\eta}\int_0^\eta \vartheta(\xi,\ y,\ t)\, \mathrm{d}y. \tag{20}$$

We will show in the next section that the zeroth-order temperature $\vartheta^{(0)}$ is the averaged temperature in the film while the higher-order terms, $\vartheta^{(n)}$ with $n \geqslant 1$, can be seen as fluctuations around the mean with zero mean [63].

(5) The last step is to check that, at each order, the existence and uniqueness of the solution is guaranteed. This requirement – also known as Fredholm alternative [64] and compatibility or solvability condition – states that the boundary-value problem at each order has zero average over $[0; \eta]$. So far, several strategies have been proposed to ensure the compatibility condition [65]: adopting a moving reference frame with stretched length scales [39,40,49,66]; expanding variables over multiple time coordinates [63,67]; or adding and subtracting tailored advective terms [43,45,60,68]. In this work, we follow the latter approach.

(6) As a result of steps (i)–(iv), we obtain that, for certain combinations of the dimensionless parameters (Pe, Br, $\mathcal{K}$), it is possible to decouple the heat transfer between the axial and the transverse directions, and, therefore, an effective model can be formulated in terms of the averaged temperature. These conditions can be summarized in an applicability map [in terms of the exponents defined in Eq. (18)], which rigorously define conditions where the one dimensional description of forced convection in the film holds or not.

B. Derivation of the effective model

Following the procedure described in Sec. III A, we expand the variables in a power series in ε^{2-p} as in Eq. (19) into the energy balance (10)

$$\begin{aligned}
&\varepsilon^{2-p}\,\partial_t\vartheta^{(0)} + \varepsilon^{2(2-p)}\,\partial_t\vartheta^{(1)} + \varepsilon^{2-p}(u-1)\partial_\xi\vartheta^{(0)} + \varepsilon^{2(2-p)}(u-1)\partial_\xi\vartheta^{(1)}\\
&\quad + \varepsilon^{2-p}\,v\,\partial_y\vartheta^{(0)} + \varepsilon^{2(2-p)}\,v\,\partial_y\vartheta^{(1)}\\
&= \varepsilon^2\,\partial_{\xi\xi}\vartheta^{(0)} + \partial_{yy}\vartheta^{(0)} + \varepsilon^{2-p}\,\partial_{yy}\vartheta^{(1)} + \varepsilon^{2(2-p)}\,\partial_{yy}\vartheta^{(2)} + \varepsilon^{2-p+b}\,\Phi + \cdots,
\end{aligned} \tag{21a}$$

and its boundary conditions (13) and (15) at the channel wall

$$\partial_y\vartheta^{(0)}|_{y=0} + \varepsilon^{2-p}\,\partial_y\vartheta^{(1)}|_{y=0} + \varepsilon^{2(2-p)}\,\partial_y\vartheta^{(2)}|_{y=0} + \cdots = \nu\,\varepsilon^{2-p}, \tag{21b}$$

and at the fluid-gas interface

$$\begin{aligned}
&\partial_y\vartheta^{(0)}|_{y=\eta} + \varepsilon^{2-p}\,\partial_y\vartheta^{(1)}|_{y=\eta} + \varepsilon^{2(2-p)}\,\partial_y\vartheta^{(2)}|_{y=\eta} - \varepsilon^k\,\partial_y\vartheta_{\rm gas}|_{y=\eta} +\\
&\quad - \varepsilon^2\,\partial_\xi\eta\,\partial_\xi\vartheta^{(0)}|_{y=\eta} - \varepsilon^{4-p}\,\partial_\xi\eta\,\partial_\xi\vartheta^{(1)}|_{y=\eta} + \varepsilon^{k+2}\,\partial_\xi\eta\,\partial_\xi\vartheta_{\rm gas}|_{y=\eta} + \cdots = 0,
\end{aligned} \tag{21c}$$

where the order of magnitude of the governing parameters (i.e., the exponents p, b, k) has been chosen to keep the maximum number of terms at each order [69–71]. Note that in this section we use a compact notation for time and spatial derivatives for the sake of brevity.

1. Leading order

At the leading order, the boundary value problem for $\vartheta^{(0)}$ is homogeneous,

$$\begin{cases}
\partial_{yy}\vartheta^{(0)} = 0, & (22a)\\
\partial_y\vartheta^{(0)} = 0 \quad \text{at} \quad y = 0, & (22b)\\
\partial_y\vartheta^{(0)} = 0 \quad \text{at} \quad y = \eta, & (22c)
\end{cases}$$

ensuring that it admits a solution independent of y, namely, $\vartheta^{(0)}(\xi, t) = \langle\vartheta\rangle(\xi, t)$. This means that the zeroth-order temperature is the averaged temperature in the film; see Eq. (20). This is true as long as $0 \leqslant p < 2$ (or $1 \leqslant \mathrm{Pe} \ll \varepsilon^{-2}$) and $b \geqslant 0$ (or $\mathrm{Br} \leqslant 1$), meaning that thermal transport has to take place within the dispersive time window, and viscous dissipation has to enter the problem as an $\mathcal{O}(\varepsilon^{2-p})$ contribution or lower.

By inspection of the expanded boundary condition (21c), we impose an additional constraint as $k > 2(2-p)$, or $\mathcal{K} \ll (\varepsilon^2\mathrm{Pe})^2$, that reduces the model to a one–sided formulation. In other words, the gas-liquid interface is assumed to be adiabatic and the bubble temperature field ϑ_{gas} enters the problem only beyond the order $\mathcal{O}(\varepsilon^{2(2-p)})$.

2. Next order

Since the leading-order problem is homogeneous, i.e., $\vartheta^{(0)} = \langle\vartheta\rangle(\xi, t)$, the term $\partial_y \vartheta^{(0)}$ in Eq. (21a) vanishes, and, at the next order $\mathcal{O}(\varepsilon^{2-p})$, we find the following equation for $\vartheta^{(1)}$:

$$\begin{cases} \partial_t \vartheta^{(0)} + (u-1)\,\partial_\xi \vartheta^{(0)} \;=\; \partial_{yy}\vartheta^{(1)} + \varepsilon^b\,\Phi, & (23a)\\ \partial_y \vartheta^{(1)} = \nu \quad \text{at} \quad y = 0, & (23b)\\ \partial_y \vartheta^{(1)} = \varepsilon^p\,\partial_\xi\eta\,\partial_\xi\vartheta^{(0)} \quad \text{at} \quad y=\eta. & (23c)\end{cases}$$

According to the solvability condition (see Sec. III A), a solution exists if and only if the partial differential equation (23a) has zero average over $[0;\,\eta]$. To satisfy this requirement, we follow the strategy from Rubinstein and Mauri [43], Mikelić *et al.* [68], decomposing the axial velocity as follows:

$$u - 1 = \underbrace{u - \langle u\rangle}_{\text{(a)}} + \underbrace{\langle u\rangle - 1}_{\text{(b)}}, \tag{24}$$

to isolate its deviation around the mean, (a), which has zero average, from the remaining part, (b), which is uniform in y. After making such decomposition, by averaging Eq. (23a) over the film and applying the boundary conditions (23b) and (23c), we obtain

$$\partial_t\vartheta^{(0)} + (\langle u\rangle - 1)\partial_\xi\vartheta^{(0)} - \eta^{-1}(\varepsilon^p\,\partial_\xi\eta\,\partial_\xi\vartheta^{(0)} - \nu) - \varepsilon^b\,\langle\Phi\rangle = 0. \tag{25}$$

Unfortunately, the solvability condition via the identity (25) is not satisfied because the boundary and initial data are incompatible [60]. Therefore, the strategy proposed by Rubinstein and Mauri [43] is to relax (25) by assuming that such equation is satisfied only up to $\mathcal{O}(\varepsilon^{(2-p)})$, namely,

$$\underbrace{\partial_t\vartheta^{(0)} + (\langle u\rangle - 1)\partial_\xi\vartheta^{(0)}}_{\mathcal{R}_{\text{lhs}}} = \underbrace{\eta^{-1}(\varepsilon^p\,\partial_\xi\eta\,\partial_\xi\vartheta^{(0)} - \nu) + \varepsilon^b\,\langle\Phi\rangle}_{\mathcal{R}_{\text{rhs}}} + \mathcal{O}(\varepsilon^{(2-p)}), \tag{26}$$

or, in other words, that the residual is small, $\mathcal{R} = \mathcal{R}_{\text{lhs}} - \mathcal{R}_{\text{rhs}} = \mathcal{O}(\varepsilon^{(2-p)})$, and jumps to the next order. Specifically, we make use of the solvability condition, first, isolating the second-order term in Eq. (23a) and using the velocity decomposition (24) as

$$\partial_{yy}\vartheta^{(1)} = \underbrace{\partial_t\vartheta^{(0)} + (\langle u\rangle - 1)\,\partial_\xi\vartheta^{(0)}}_{\mathcal{R}_{\text{lhs}}} + (u - \langle u\rangle)\,\partial_\xi\vartheta^{(0)} - \varepsilon^b\,\Phi, \tag{27}$$

and, then, replacing $\mathcal{R}_{\text{lhs}}$ with $\mathcal{R}_{\text{rhs}}$ in Eq. (27) using Eq. (26), leading to a regularized boundary boundary value problem

$$\partial_{yy}\vartheta^{(1)} = (u - \langle u\rangle)\partial_\xi\vartheta^{(0)} - \varepsilon^b(\Phi - \langle\Phi\rangle) + \eta^{-1}(\varepsilon^p\,\partial_\xi\eta\,\partial_\xi\vartheta^{(0)} - \nu) + \mathcal{O}(\varepsilon^{(2-p)}), \tag{28}$$

where the residual of the order of $\mathcal{O}(\varepsilon^{(2-p)})$ jumps to the next order.

The solution is finally obtained by integrating Eq. (28) twice and the two integration constants are found using either Eq. (23b) or Eq. (23c), together with the zero-average gauge condition, i.e., $\langle\vartheta^{(1)}\rangle = 0$. This gives the solution for the order one term of the asymptotic expansion as

$$\vartheta^{(1)}(\xi,\,y,\,t) = (\mathcal{M}_a + \varepsilon^p\,\partial_\xi\eta\,\mathcal{M}_\Gamma)\partial_\xi\vartheta^{(0)} + \varepsilon^b\,\mathcal{M}_\Phi + \nu\,\mathcal{M}_q, \tag{29}$$

where the following B-fields (named after Ref. [72])

$$\mathcal{M}_a = \frac{(\eta-1)(8\,\eta^4 - 60\,\eta^2\,y^2 + 60\,\eta\,y^3 - 15\,y^4)}{120\,\eta^3}, \quad \mathcal{M}_\Gamma = \frac{3\,y^2 - \eta^2}{6\,\eta}, \tag{30a}$$

$$\mathcal{M}_\Phi = \frac{(\eta-1)^2(8\,\eta^4 - 60\,\eta^2\,y^2 + 60\,\eta\,y^3 - 15\,y^4)}{20\,\eta^6}, \quad \mathcal{M}_q = -\frac{2\,\eta^2 - 6\,\eta\,y + 3\,y^2}{6\,\eta}, \tag{30b}$$

describe the effective contributions of advection ($\mathcal{M}_a$), film shape ($\mathcal{M}_\Gamma$), viscous dissipation ($\mathcal{M}_\Phi$), and wall heat flux ($\mathcal{M}_q$).

3. *Next next order*

At the next next order $\mathcal{O}(\varepsilon^{2(2-p)})$, the boundary value problem for $\vartheta^{(2)}$ from (21a), plus the the residual $\mathcal{R}$ defined in Eq. (26) and resulting from the solvability condition of the previous order, is given by

$$\begin{cases} \partial_t \vartheta^{(1)} + (u-1)\,\partial_\xi \vartheta^{(1)} + v\,\partial_y \vartheta^{(1)} + \varepsilon^{p-2}\,\mathcal{R} = \partial_{yy}\vartheta^{(2)} + \varepsilon^{2p-2}\,\partial_{\xi\xi}\vartheta^{(0)}, & \text{(31a)} \\ \partial_y \vartheta^{(2)} = 0 \quad \text{at} \quad y = 0, & \text{(31b)} \\ \partial_y \vartheta^{(2)} = \varepsilon^p\,\partial_\xi \eta\,\partial_\xi \vartheta^{(1)} \quad \text{at} \quad y = \eta. & \text{(31c)} \end{cases}$$

Since we are interested only in deriving an effective equation for the averaged temperature, it not necessary to solve for $\vartheta^{(2)}$, but it is sufficient to enforce the solvability condition on Eq. (31). Specifically, we replace $\vartheta^{(1)}$ using the solution at the previous order (29), and, then, depth-average the equation (31a) using its boundary conditions (31b) and (31c). By doing so, the terms that are independent of y remain unchanged, while the average of the time derivative is zero since the film profile is a function of the axial coordinate only yielding $\langle \partial_t \vartheta^{(1)} \rangle = \partial_t \langle \vartheta^{(1)} \rangle = 0$.

The result of the average is an advection-diffusion-heat-transfer equation for the zeroth-order temperature (or the averaged temperature)

$$\frac{\partial \vartheta^{(0)}}{\partial t} + (u^\star - 1)\frac{\partial \vartheta^{(0)}}{\partial \xi} = \varepsilon^p D^\star \frac{\partial^2 \vartheta^{(0)}}{\partial \xi^2} + \varepsilon^b\,\Phi^\star - \nu\,q^\star, \tag{32}$$

where the effective coefficients for advection, diffusion, viscous heating, and the imposed flux are defined as

$$u^\star = u_0 + \varepsilon^2 \sum_{i=1}^{8} u_i + u_9, \quad D^\star = 1 + \varepsilon^2 \sum_{i=0}^{3} D_i, \quad \Phi^\star = \Phi_0 + \varepsilon^2 \sum_{i=1}^{3} \Phi_i, \quad q^\star = q_0 + \varepsilon^2 \sum_{i=1}^{3} q_i, \tag{33}$$

with the full expressions reported in Table I.

C. One-dimensional advection-diffusion-heat-transfer equation and the applicability conditions

To sum up, the procedure, outlined schematically in Fig. 2(a), yields a one-dimensional advection-diffusion-heat-transfer equation for the averaged temperature in the film:

$$\frac{\partial \langle \vartheta \rangle}{\partial t} + (u^\star - 1)\frac{\partial \langle \vartheta \rangle}{\partial \xi} = \frac{D^\star}{\mathrm{Pe}} \frac{\partial^2 \langle \vartheta \rangle}{\partial \xi^2} + \mathrm{Br}\,\Phi^\star - \nu\,q^\star, \tag{34}$$

where $u^\star$, $D^\star$, $\Phi^\star$ and $q^\star$ denote the effective advection, diffusivity, viscous dissipation, and heat flux coefficients, respectively. Their full expressions are provided in Table I and Eq. (33).

As outlined in the derivation, Eq. (34) holds only for a specific range of the dimensionless groups, namely,

$$\text{(a)}\ \ \varepsilon \ll 1, \quad \text{(b)}\ \ 1 \leqslant \mathrm{Pe} \ll \varepsilon^{-2}, \quad \text{(c)}\ \ \mathrm{Br} \leqslant 1, \quad \text{(d)}\ \ \mathcal{K} \ll (\varepsilon^2\,\mathrm{Pe})^2. \tag{35}$$

Such criteria provide sufficient conditions for the effective model to describe the averaged temperature field asymptotically, and the corresponding applicability map is shown in Fig. 2(b). Specifically, (a) ensures the use of the lubrication approximation in the thin film; (b) bounds the Péclet number based on the dispersive timescale hierarchy, i.e., $\mathcal{T}_{d,h} \ll \mathcal{T}_a < \mathcal{T}_{d,L}$; (c) limits the shear heating; (d) ensures that the temperature field in the film is decoupled with respect to the one inside the bubble (i.e., the one-sided formulation) enforcing that the bubble temperature contributes only at higher orders (beyond $n = 2$, up to which model consistency is guaranteed).

TABLE I. Effective coefficients, according to Eq. (33). Each contribution u_i (top tables), D_i, Φ_i, q_i (bottom table) is expressed as the product of a "Shape" and a "Type" term. Specifically, "Shape" is a function of the local film thickness only; "Type" is the driving term that captures the effect of the Péclet number, the interface concavity ($\partial_{\xi\xi}\eta$) and slope ($\partial_\xi \eta$). To isolate the impact of the latter, the transverse velocity is written as $v \equiv v^\dagger\, \partial_\xi \eta$, see Eq. (C1); the film-relative velocity is indicated by prime notation, i.e., $u' \equiv u - 1$. The column "Mechanism" identifies the physical origin of each term; mechanisms denoted with a single ($*$) or double ($**$) asterisk correspond to the regularizing boundary conditions (23b) and (23c), respectively.

$u^\star$	Mechanism	Shape	Type	$u^\star$	Mechanism	Shape	Type
u_0	$\langle u\rangle$	$\dfrac{\eta-1}{\eta}$	1	u_3	$\langle u'\,\partial_\eta \mathcal{M}_\Gamma\rangle$	$\dfrac{47-7\,\eta}{120\,\eta}$	$\partial_\xi^2 \eta$
u_9	$**$	$-\dfrac{1}{\eta}$	$\partial_\xi \eta\,\mathrm{Pe}^{-1}$	u_4	$\langle v^\dagger\,\partial_y \mathcal{M}_\Gamma\rangle$	$\dfrac{7\,\eta-18}{40\,\eta}$	$\partial_\xi^2 \eta$
u_1	$\langle u'\,\partial_\eta \mathcal{M}_a\rangle$	$-\dfrac{(\eta-1)(24\,\eta+41)}{840\,\eta}$	$\partial_\xi \eta\,\mathrm{Pe}$	u_5	$-\eta^{-1}\partial_\eta \mathcal{M}_a\vert_\eta$	$\dfrac{7(2\,\eta-1)}{120\,\eta}$	$\partial_\xi^2 \eta$
u_2	$\langle v^\dagger\,\partial_y \mathcal{M}_a\rangle$	$\dfrac{(\eta-1)(19-8\,\eta)}{280\,\eta}$	$\partial_\xi \eta\,\mathrm{Pe}$	u_7	$-\eta^{-1}\partial_\eta \mathcal{M}_\Gamma\vert_\eta$	$\dfrac{2}{3\,\eta}$	$\partial_\xi^3 \eta\,\mathrm{Pe}^{-1}$
u_6	$\langle u'\,\mathcal{M}_\Gamma\rangle$	$\dfrac{7(\eta-1)}{120}$	$\partial_{\xi\xi}\eta$	u_8	$-\eta^{-1}\mathcal{M}_\Gamma\vert_\eta$	$-\dfrac{1}{3}$	$\partial_\xi \eta\,\partial_{\xi\xi}\eta\,\mathrm{Pe}^{-1}$

$D^\star$	Mechanism	Shape	$\Phi^\star$	Mechanism	Shape	$q^\star$	Mechanism	Shape	Type
D_0	$-\langle u'\,\mathcal{M}_a\rangle$	$\dfrac{2(\eta-1)^2}{105}$							Pe^2
			Φ_0	$\langle\Phi\rangle$	$\dfrac{3\,(\eta-1)^2}{\eta^4}$	q_0	$*$	$\dfrac{1}{\eta}$	1
D_1	$-\langle u'\,\mathcal{M}_\Gamma\rangle$	$-\dfrac{7(\eta-1)}{120}$	Φ_1	$-\langle u'\,\partial_\eta \mathcal{M}_\Phi\rangle$	$\dfrac{(\eta-1)^2(89-8\,\eta)}{140\,\eta^4}$	q_1	$\langle u'\,\partial_\eta \mathcal{M}_q\rangle$	$\dfrac{7\,\eta+13}{120\,\eta}$	$\partial_\xi \eta\,\mathrm{Pe}$
D_2	$\eta^{-1}\mathcal{M}_a\vert_\eta$	$-\dfrac{7(\eta-1)}{120}$	Φ_2	$-\langle v^\dagger\,\partial_y \mathcal{M}_\Phi\rangle$	$\dfrac{3(\eta-1)^2(8\,\eta-19)}{140\,\eta^4}$	q_2	$\langle v^\dagger\,\partial_y \mathcal{M}_q\rangle$	$\dfrac{3\,\eta-7}{40\,\eta}$	$\partial_\xi \eta\,\mathrm{Pe}$
D_3	$\eta^{-1}\mathcal{M}_\Gamma\vert_\eta$	$\dfrac{1}{3}$	Φ_3	$\eta^{-1}\partial_\eta \mathcal{M}_\Phi\vert_\eta$	$-\dfrac{7(\eta-1)}{10\,\eta^4}$	q_3	$-\eta^{-1}\partial_\eta \mathcal{M}_q\vert_\eta$	$-\dfrac{1}{6\,\eta}$	$\partial_\xi^2 \eta$

D. Numerical solution and boundary conditions of the effective model

The numerical solution of Eq. (34) requires the evolution of the film profile, since it shapes its effective coefficients. Specifically, $\eta(\xi)$ is obtained solving Eq. (1) separately for the rear and front menisci, using MATLAB's ordinary differential equation (ODE) solver `ode45` as outlined in Refs. [45,55]. Setting the length L of the transition regions at the front and rear to $\Delta l_{\mathrm{front}} = \Delta l_{\mathrm{rear}} = 15$, we get the corresponding film menisci as shown in Fig. 9. This choice ensures that the second derivative of the interface profile converges to its asymptotic value, $\mathrm{d}^2\eta/\mathrm{d}\xi^2 \to 0.643$ when $|\xi| = \mathcal{O}(\Delta l_{\mathrm{front}}) = \mathcal{O}(\Delta l_{\mathrm{rear}})$, allowing the computed menisci to match the fore and aft spherical cap, respectively. An additional region of uniform thickness (where $\eta = 1$) of length l can be artificially introduced between the front and the rear extending the studied domain of $l/2$ on either side of $\xi = 0$ to analyze the impact of the bubble length on the averaged Nusselt number as in Sec. IV C. An example of the overall film profile obtained in this way is shown in Fig. 1.

Given the bubble shape, the equation (34) is solved numerically using MATLAB's built-in one-dimensional partial differential equation (PDE) solver `pdepe`. Such solver employs a second-order accurate spatial discretization to convert the original problem into a system of ODEs, and integrates them by dynamically adapting both the time step and the order of the scheme [73]. A uniform mesh with spacing $\Delta\xi \approx 0.089$ is used to resolve the film region, while the relative and absolute time-integration tolerances are set to 10^{-8} to ensure high accuracy. The boundary and initial conditions for the averaged temperature $\langle\vartheta\rangle$ are determined via the energy balance in the channel ahead and

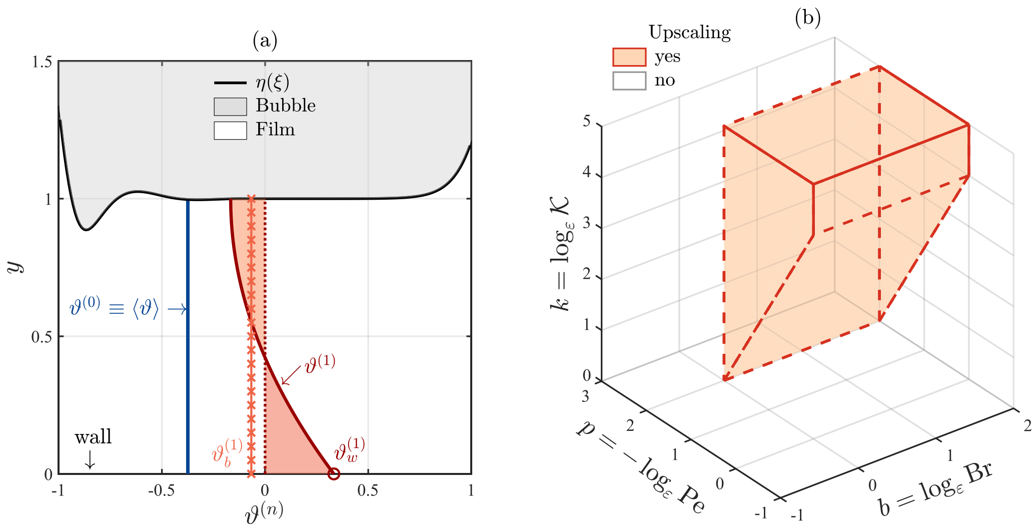

FIG. 2. (a) Schematic of the upscaling technique, representing the temperature in the film domain $y \in [0; \eta(\xi)]$ as the sum of a uniform leading-order variable $\vartheta^{(0)} \equiv \langle\vartheta\rangle$ corrected by zero-mean higher-order fluctuations $\vartheta^{(n)}$. The first-order corrections ($n = 1$), the wall (w) and the bulk temperature (b) are plotted. (b) Applicability map showing the region of the parameter space (p, b, k) where the effective model (34) is valid, see Eqs. (35) and (18): $0 \leqslant p < 2$, $b \geqslant 0$, and $k > 2(2 - p)$.

behind of the elongated bubble and is described in the next section. The error estimate is presented in Appendix D, where we compare the numerical solution of (34) with the solution of the full two-dimensional problem (10).

1. Initial and boundary condition for the averaged temperature

To find the initial and the boundary conditions for the averaged temperature in the thin film, the idea is to match the film averaged temperature with the averaged temperature in the channel ahead and behind. To do so, we write the energy balance under thermally fully developed conditions in the liquid ahead of or behind the bubble [74] assuming that the portion of the channel considered is much greater than the channel half width. Specifically, we consider an infinitesimal slice of the channel in regimes where convective heat transport dominates over axial conduction in the channel and viscous dissipation is neglected. Thus, the net heat transferred over an small portion of the channel $\delta\hat{x}$ with respect to the laboratory reference frame is given by

$$\delta q = \dot{m}\, c_p\, (\hat{T}_b|_{\hat{x}+\delta\hat{x}} - \hat{T}_b|_{\hat{x}}), \tag{36}$$

where $\dot{m}$ is the mass flow rate and $\hat{T}_b$ is the bulk temperature; the heat transferred from the wall to the fluid is given by $\delta q = -q_w''\, \mathcal{P}\, \delta\hat{x}$ with $\mathcal{P}$ the wetted perimeter of the channel cross-sectional area $\mathcal{A}$. Combining the definition of the mass flow rate, $\dot{m} = \rho_f\, \mathcal{A}\, U_\infty$ with that of the thermal diffusivity α_f, and taking the limit $\delta\hat{x} \to 0$, the energy balance (36) is recast in the differential form

$$\frac{\mathrm{d}\hat{T}_b}{\mathrm{d}\hat{x}} = -\frac{q_w''}{U_\infty}\, \frac{\mathcal{P}}{\mathcal{A}}\, \frac{\alpha_f}{\kappa_f}. \tag{37}$$

Under uniform heating conditions, the right-hand side of (37) is independent of $\hat{x}$, highlighting that the bulk temperature of the liquid varies linearly with the axial coordinate. The geometrical factor $\mathcal{P}/\mathcal{A}$ equals $1/R$ or $2/R$ for a planar channel and a cylindrical tube, respectively, yielding $\mathcal{P}/\mathcal{A} = (1 + m)/R$. Since the bulk and the averaged temperature differ by at most $\mathcal{O}(\varepsilon^2\, \mathrm{Pe})$, we assume that $\langle\vartheta\rangle \approx \vartheta_b$; see Eq. (41).

Then, introducing the dimensionless bulk temperature ϑ_b via (9) and the axial coordinate (in the laboratory reference frame) $x = \hat{x}/L$, and using relations (3) and (4) the energy balance (37) reads

$$\frac{\mathrm{d}\langle\vartheta\rangle}{\mathrm{d}x} \approx \frac{\mathrm{d}\vartheta_b}{\mathrm{d}x} = -\frac{\nu(1+m)0.643\,\varepsilon^2}{1-(1+m)0.643\,\varepsilon^2}, \tag{38}$$

where we see that the slope of the bulk temperature is small and of the order of $\mathcal{O}(\varepsilon^2)$.

The initial and boundary conditions of the effective model are obtained by integrating Eq. (38), and setting the integration constant to zero, consistent with the initial condition (17) at $\langle\vartheta\rangle|_{x=0} = 0$. Specifically, we impose the following Dirichlet boundary conditions at the the right and left boundaries of the film domain

$$\langle\vartheta\rangle|_{\xi} = -\frac{\nu(1+m)0.643\,\varepsilon^2}{1-(1+m)\,0.643\,\varepsilon^2}(\xi+t), \tag{39}$$

where we shift from the laboratory to the moving reference frame via $x = \xi + t$. Evaluating Eq. (39) at $t = 0$ yields the initial condition.

IV. RESULTS AND DISCUSSION

In this section, we discuss the ramifications of the effective model to understand why the presence of an elongated bubble enhances heat transfer under uniform heating conditions, identifying the key physical mechanisms and the scaling of the Nusselt number for this problem.

A. Effective heat-transfer coefficients and averaged temperature field

Figure 3 shows the impact of the Péclet number on the effective coefficients appearing in Eq. (34), ranging from $\mathrm{Pe} = \mathcal{O}(1)$ (diffusion-dominated regime) to the limiting case $\mathrm{Pe} = \mathcal{O}(\varepsilon^{-2})$ (advection-dominated). Those coefficients strongly depend on the shape of the meniscus, suggesting that different regions of the film (i.e., the uniform film, the front and the rear) may contribute differently to the overall heat transfer. Each of them originates from averaging the velocity profile and the Brenner's functions as summarized in Table I: this means that it is possible to rigorously track back the physical mechanism responsible of an enhancement or a reduction of the effective coefficients.

The effective advection coefficient $u^\star$, shown in Fig. 3(a), is the sum of the pure advection in the axial direction (u_0 in Table I), the imposed heat-flux at the channel wall (u_9), advection in both axial and traverse directions via the Brenner's function (u_1, u_2, and u_5), the combined effect of axial and traverse advection and the Brenner's function due to the boundary conditions (u_3, u_4, u_6, u_7, and u_8). Interestingly, $u^\star$ is negligible only in the uniform film region, where the capillary driving force is negligible and the fluid is at rest, i.e., $\mathrm{d}^3\eta/\mathrm{d}\xi^3 = 0$ in Eq. (1) when $\eta = 1$. Instead, the shape oscillations at the bubble rear induce changes in its sign since the advective contributions to $u^\star$ (see u_1 and u_2 in Table I) are proportional to the derivative of the bubble shape, $\propto -\eta\,\partial_\xi\eta\,\mathrm{Pe}$. As a result, the effective advection increases with the Péclet number at the bubble rear, while at the front it exhibits a nonmonotonic behavior—particularly in the advection-dominated regime—due to the competition between advection and the imposed heat flux.

In the uniform film region the energy is transported purely by thermal diffusion, and the effective diffusion coefficient $D^\star$ equals unity, as shown in Fig. 3(b). In the transition regions, instead, there is a net flow in the axial and transverse direction (see the streamlines in Fig. 9) that enhances the effective diffusion coefficient at sufficiently large Péclet numbers. The leading contribution to $D^\star$ (denoted as D_0 in Table I) follows the scaling law typical of the Aris-Taylor dispersion—a quadratic dependence on the film-scale Péclet number—with a numerical prefactor equal to the theoretical limit for plane Poiseuille flow, $2/105$. The evolution of the effective thermal diffusion coefficient is similar to the one obtained for the transport of a passive scalar in a thin film in Picchi and Poesio [45].

The effective coefficient accounting for viscous dissipation $\Phi^\star$, shown in Fig. 3(c), is only weakly dependent on Pe. Specifically, the leading contribution to $\Phi^\star$ (denoted as Φ_0 in

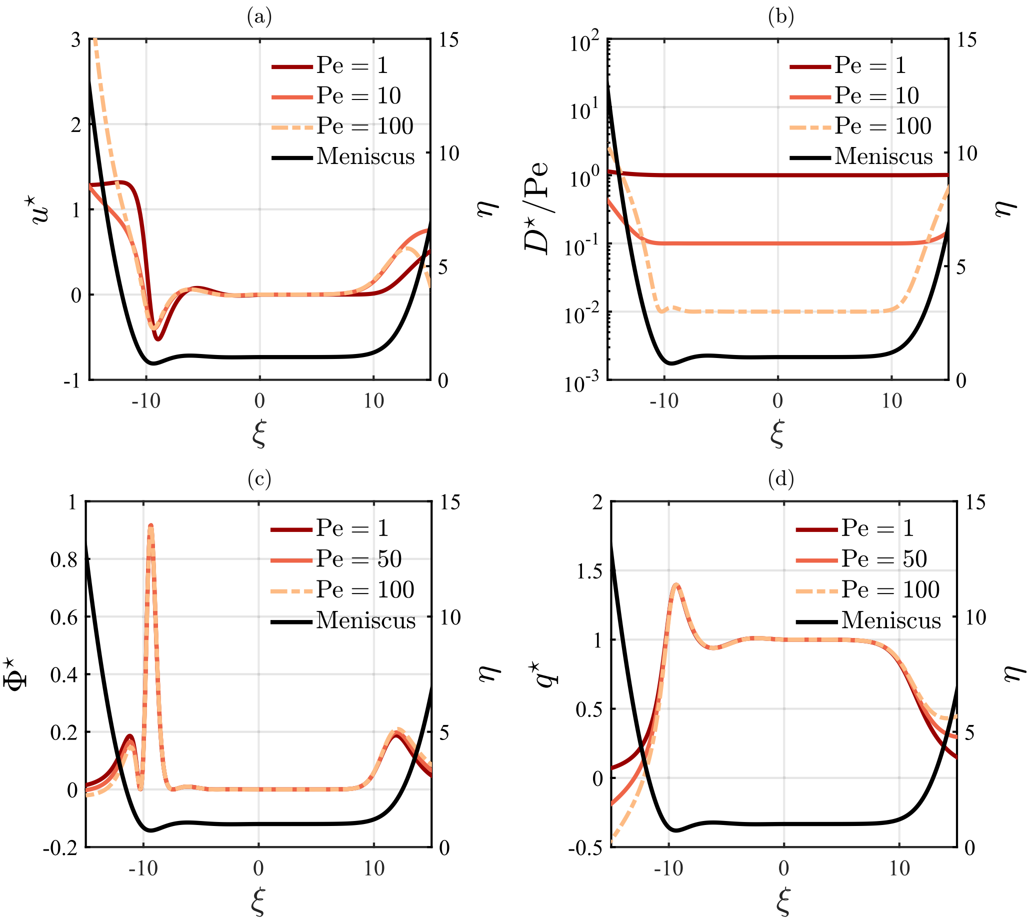

FIG. 3. Impact of the Péclet (Pe) number on the model effective coefficients, see Eq. (33), for advection, diffusion, viscous dissipation, and heat flux as functions of the axial coordinate ξ: (a) $u^\star$, (b) $D^\star/\mathrm{Pe}$, (c) $\Phi^\star$, (d) $q^\star$; right, meniscus profile $\eta(\xi)$. The small-scale parameter is set to $\varepsilon = 0.1$, corresponding to $\mathrm{Ca} \approx 3.33 \times 10^{-4}$.

Table I) takes the form of a quadratic expression $\propto (\eta - 1)^2/\eta^4$, that can be seen as the product of the pressure gradient, $(\eta - 1)/\eta^3$, and the averaged speed, $(\eta - 1)/\eta$, in the thin film, obtained via the lubrication theory [3,55]. This is the typical form of the viscous dissipation or the entropy production (when divided by the temperature) of a fluid flow in a confined geometry [75]. The viscous dissipation is maximal in the front (there is a region near the nose where the pressure gradient is maximal) and in the rear corresponding to the meniscus undulations where local recirculation vortices are present, see the streamlines in Fig. 9.

Similarly, the leading contribution to the effective heat source term $q^\star$ (denoted as q_0 in Table I) scales as the inverse of the film thickness, $q_0 \sim \eta^{-1}$, suggesting that heat transfer is enhanced in regions where the fluid layer is smaller, namely, the uniform film region and the bubble's rear, as shown in Fig. 3(d). Higher Péclet numbers simultaneously increase $q^\star$ at the front and decrease it at the rear: when advection prevails, in fact, the velocity field tends to locally accumulate heat in the front, while removing it from the bubble's rear, see the streamlines in Fig. 7(b).

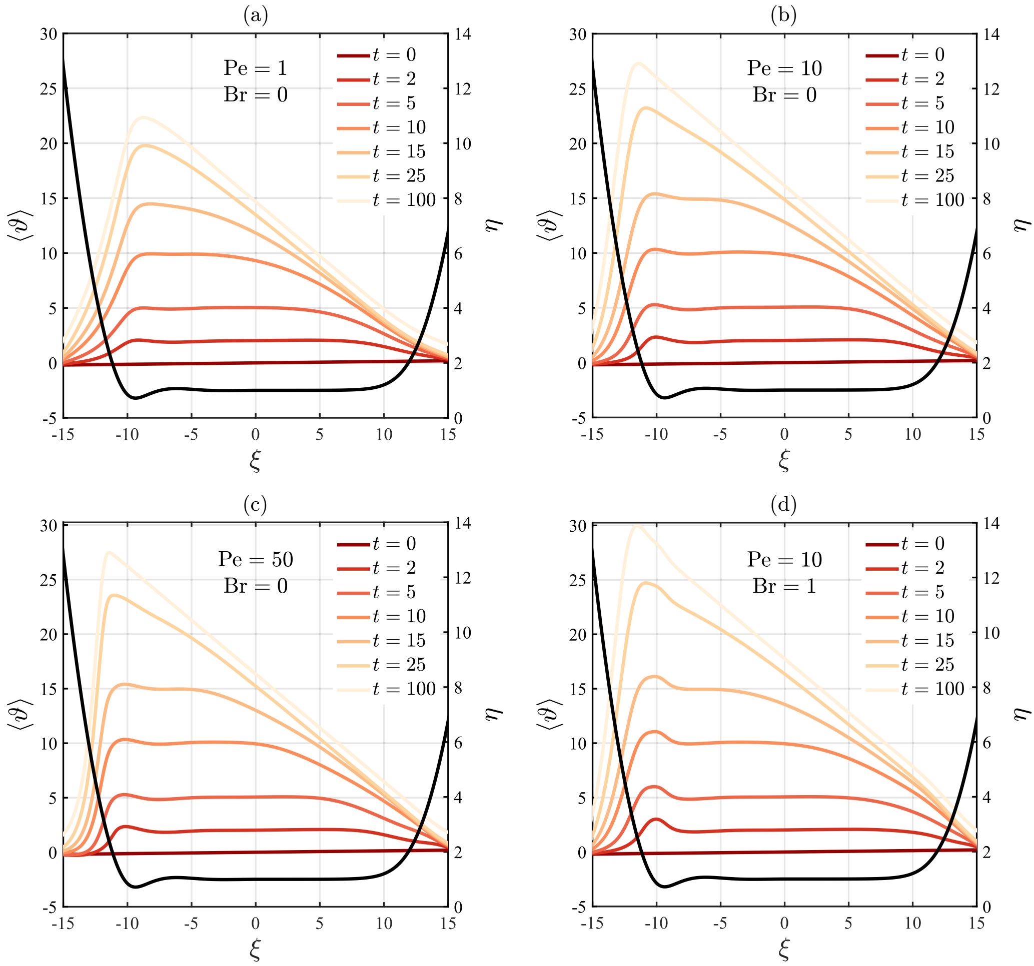

FIG. 4. Impact of the Péclet (Pe) and Brinkman (Br) numbers on the mean film temperature $\langle\vartheta\rangle$ in a cylindrical tube ($m = 1$), under inward heat flux conditions ($\nu = -1$), as a function of the axial coordinate ξ, evaluated at fixed time instants t: (a) $\mathrm{Pe} = 1$, (b) $\mathrm{Pe} = 10$, and (c) $\mathrm{Pe} = 50$, with $\mathrm{Br} = 0$; in panel (d) $\mathrm{Pe} = 10$ and $\mathrm{Br} = 1$; right, meniscus profile $\eta(\xi)$. The small-scale parameter is set to $\varepsilon = 0.1$, corresponding to $\mathrm{Ca} \approx 3.33 \times 10^{-4}$.

Figure 4 shows the evolution of the averaged temperature field obtained solving numerically (34) as described in Sec. III D for the case of a cylindrical tube heated uniformly from the wall. The chosen time interval corresponds to the onset of thermally fully developed conditions in the reference frame attached to the bubble. At early times, the temperature increases almost uniformly along the central portion of the bubble, while, as time elapses, the temperature profile becomes almost linear in the thin film region. Under conditions of imposed uniform heat flux, a steady-state solution for the averaged temperature field in the moving reference frame cannot be achieved since the film is continuously heated from the solid boundary. However, a fully developed heat transfer coefficient is reached once the difference between the bulk and the wall temperatures becomes independent of the axial coordinate [74], as it will be discussed in detail in Sec. IV B.

As shown in Figs. 4(a)–4(c), increasing the Péclet number leads to a sharper temperature gradient at the rear of the bubble and amplifies the peak located at the point of minimum film thickness. This is consistent with fluid recirculation in the bubble's rear (see Fig. 9), which increases the residence time of a fluid particle being continuously heated from the wall. A similar trend is observed in regimes where viscous dissipation plays a role: comparing Figs. 4(b) and 4(d), which differ only in the Brinkman number, we see that viscus heating amplifies both the height of the triangular profile and the magnitude and width of the peak, but, overall, the temperature profiles look qualitatively similar.

B. Local Nusselt number

The heat-transfer enhancement induced by an elongated bubble is quantified via the local convective heat transfer coefficient, defined as the ratio between the specific heat flux entering the fluid, q''_w, and the difference between the wall temperature and the bulk temperature [49,57,74,76], that, in terms of the dimensionless variables defined in Sec. II C, yields

$$h = -\nu \, \frac{\kappa_f \, U_b \, h_\infty}{\alpha_f \, L(\vartheta_w - \vartheta_b)}, \tag{40}$$

where $\vartheta_w \equiv \vartheta|_{y=0}$ is the dimensionless wall temperature and ϑ_b is the dimensionless bulk temperature. The latter is defined as an enthalpy-weighted average relative to the laboratory reference frame and differs from the mean film temperature $\langle\vartheta\rangle$ due to higher-order corrections:

$$\vartheta_b \equiv \frac{\int_0^\eta u\,\vartheta\,\mathrm{d}y}{\int_0^\eta u\,\mathrm{d}y} = \langle\vartheta\rangle + \varepsilon^{2-p}\,\vartheta_b^{(1)} + \mathcal{O}(\varepsilon^{2(2-p)}), \quad \text{with} \quad \vartheta_b^{(1)} \equiv \frac{\int_0^\eta u\,\vartheta^{(1)}\,\mathrm{d}y}{\int_0^\eta u\,\mathrm{d}y}. \tag{41}$$

Such average is taken over the liquid film thickness, given its dominant heat capacity relative to the one of the gas [77]. Expanding the wall temperature, $\vartheta_w = \langle\vartheta\rangle + \varepsilon^{2-p}\,\vartheta_w^{(1)} + \mathcal{O}(\varepsilon^{2(2-p)})$, and combining Eqs. (40) and (41) we obtain a closed–form solution for the local Nusselt number based on the uniform film thickness

$$\mathrm{Nu}_x^{h_\infty} = \frac{h\,h_\infty}{\kappa_f} = -\frac{\nu}{\vartheta_w^{(1)} - \vartheta_b^{(1)}}. \tag{42}$$

This formulation of the local Nusselt number is based on the uniform film thickness as the relevant length scale for the forced convection around an elongated bubble. However, the local Nusselt number for Taylor flows is conventionally formulated using the hydraulic diameter, namely, $2(2-m)R$, instead of the uniform film thickness (see, e.g., Refs. [28,29,32]). Thus, rescaling Eq. (42) with $2(2-m)R/h_\infty$ via Eq. (3), we get the local Nusselt number based on the hydraulic diameter as

$$\mathrm{Nu}_x = -\frac{2(2-m)}{0.643(3\,\mathrm{Ca})^{2/3}}\,\frac{\nu}{\vartheta_w^{(1)} - \vartheta_b^{(1)}}. \tag{43}$$

Using Eqs. (29) and (30) and the velocity profile (C1), the first-order corrections to the wall and bulk temperature are given by

$$\vartheta_w^{(1)}(\xi,t) = \eta\left(\frac{\eta-1}{15} - \frac{1}{6\,\mathrm{Pe}}\frac{\mathrm{d}\eta}{\mathrm{d}\xi}\right)\frac{\partial\langle\vartheta\rangle}{\partial\xi} + \frac{2\,\mathrm{Br}}{5}\left(\frac{\eta-1}{\eta}\right)^2 - \nu\,\frac{\eta}{3}, \tag{44a}$$

$$\vartheta_b^{(1)}(\xi,t) = \eta\left(-\frac{2(\eta-1)}{105} + \frac{7}{120\,\mathrm{Pe}}\frac{\mathrm{d}\eta}{\mathrm{d}\xi}\right)\frac{\partial\langle\vartheta\rangle}{\partial\xi} - \frac{4\,\mathrm{Br}}{35}\left(\frac{\eta-1}{\eta}\right)^2 + \nu\,\frac{\eta}{15}, \tag{44b}$$

and these are, then, substituted into Eq. (43), yielding

$$\mathrm{Nu}_x = \frac{\mathrm{Nu}_0}{\eta(1-\nu\,\Gamma)}, \quad \text{with} \quad \mathrm{Nu}_0 = \frac{5(2-m)}{0.643(3\,\mathrm{Ca})^{2/3}}, \tag{45}$$

where Nu_0 is the Nusselt number in the uniform film region and Γ accounts for the contribution of advection and viscous dissipation as

$$\Gamma(\xi,\, t;\, \mathrm{Pe},\, \mathrm{Br}) = \left(\frac{3(\eta-1)}{14} - \frac{9}{16\,\mathrm{Pe}}\frac{\mathrm{d}\eta}{\mathrm{d}\xi}\right)\frac{\partial\langle\vartheta\rangle}{\partial\xi} + \frac{9\,\mathrm{Br}}{7}\frac{(\eta-1)^2}{\eta^3}. \tag{46}$$

To sum up, the local Nusselt number in the thin-film region surrounding an elongated, inviscid Bretherton's bubble (i.e., negligible inertial and gravitational effects) under uniform heat flux conditions depends on space and time through the film thickness, its slope, and the temperature gradient. This dependence is governed by a set of dimensionless groups—namely, the Péclet, Brinkman and capillary numbers—as well as the cross-sectional geometry and the orientation of the thermal flux, namely, $\mathrm{Nu}_x = \mathrm{Nu}_x(\eta,\, \mathrm{d}\eta/\mathrm{d}\xi,\, \partial\langle\vartheta\rangle/\partial\xi;\, \mathrm{Pe},\, \mathrm{Br},\, \mathrm{Ca};\, \nu,\, m)$. Formulated as in Eq. (45), we see that the dependence on the capillary number enters only via Nu_0, while the Nusselt number scales as the inverse of the film thickness, $\mathrm{Nu}_x \sim \eta^{-1}$, similarly to what observed for core-annular flows in Botticini *et al.* [49]. The Péclet and the Brinkman numbers only affect the term $(1-\nu\,\Gamma)$ and have a small effect on the Nusselt number.

In the uniform film region, where $\eta = 1$, $\mathrm{d}\eta/\mathrm{d}\xi = 0$, and $\Gamma = 0$, Nu_x depends only on the capillary number and the geometry of the cross-section, i.e., $\mathrm{Nu}_x = \mathrm{Nu}_0(\mathrm{Ca},\, m)$, simplifying to $\mathrm{Nu}_x \equiv \mathrm{Nu}_0 \approx 3.7383\,\mathrm{Ca}^{-2/3}$ for a cylindrical tube ($m = 1$). Therefore, viscous dissipation and temperature gradient do not affect the heat transfer coefficient in the uniform film region of the elongated bubble. There, in fact, the fluid is at rest and the thermal problem is dominated by thermal diffusion. In Appendix E, the local Nusselt number predicted by our model is compared with numerical results from the literature beyond its rigorous range of validity, indicating the dominant role of film thickness in heat transfer.

Outside the flat-film region, the evolution of the local Nusselt number is highly sensitive to both the shape of the interface and time, as shown in Fig. 5. In general, the local Nusselt number decreases over time in the rear of the bubble and increases in the front. Specifically, at low Péclet numbers—Fig. 5(a)—diffusion dominates over advection and the decay of the local Nusselt number in the rear is smooth and monotonic, while no significant temporal variation is observed in the front. As advection becomes more relevant—Fig. 5(b)—the increase of Nu_x in the front becomes more pronounced with time, suggesting the onset of convective enhancement in that region. In the strongly advection-dominated regime—Fig. 5(c)—the Nu_x profile in the rear shows a local minimum that progressively shifts toward the tip of the bubble with time, accompanied by a steepening near the point of minimum film thickness (at $\xi \approx -10$). Interestingly, in the front, the local Nusselt number increases significantly with time far from the uniform film due to the predominant advection (the effect of the transverse velocity is significant there). However, it is worth mentioning that, when $\eta \gg 1$, the profile matches the spherical cap and the thin-film approximation does not hold anymore.

Viscous heating reduces the peak in the local Nusselt number in the bubble's rear compared to the case with $\mathrm{Br} = 0$; see Fig. 5(d). This indicates a lower heat-transfer efficiency since part of the thermal energy is internally generated and is not exchanged with the solid wall.

C. Averaged Nusselt number in the thin film

A more complete characterization of forced convection in the thin film of an elongated bubble is given by the averaged Nusselt number, computed via integration of the local Nusselt number over the axial direction (see, e.g., Refs. [26,57]). Alternative averaging approaches are discussed in Appendix F.

In the following, we investigate the effect of the film length on the averaged Nusselt number distinguishing between the three sub-regions, namely, the rear, the uniform film, and the front. Thus, we introduce the average Nusselt numbers for the rear and the front as

$$\overline{\mathrm{Nu}}_{\mathrm{front}} = \frac{1}{\Delta l_{\mathrm{front}}}\int_{\mathrm{front}} \mathrm{Nu}_x(\xi)\,\mathrm{d}\xi, \quad \overline{\mathrm{Nu}}_{\mathrm{rear}} = \frac{1}{\Delta l_{\mathrm{rear}}}\int_{\mathrm{rear}} \mathrm{Nu}_x(\xi)\,\mathrm{d}\xi, \tag{47}$$

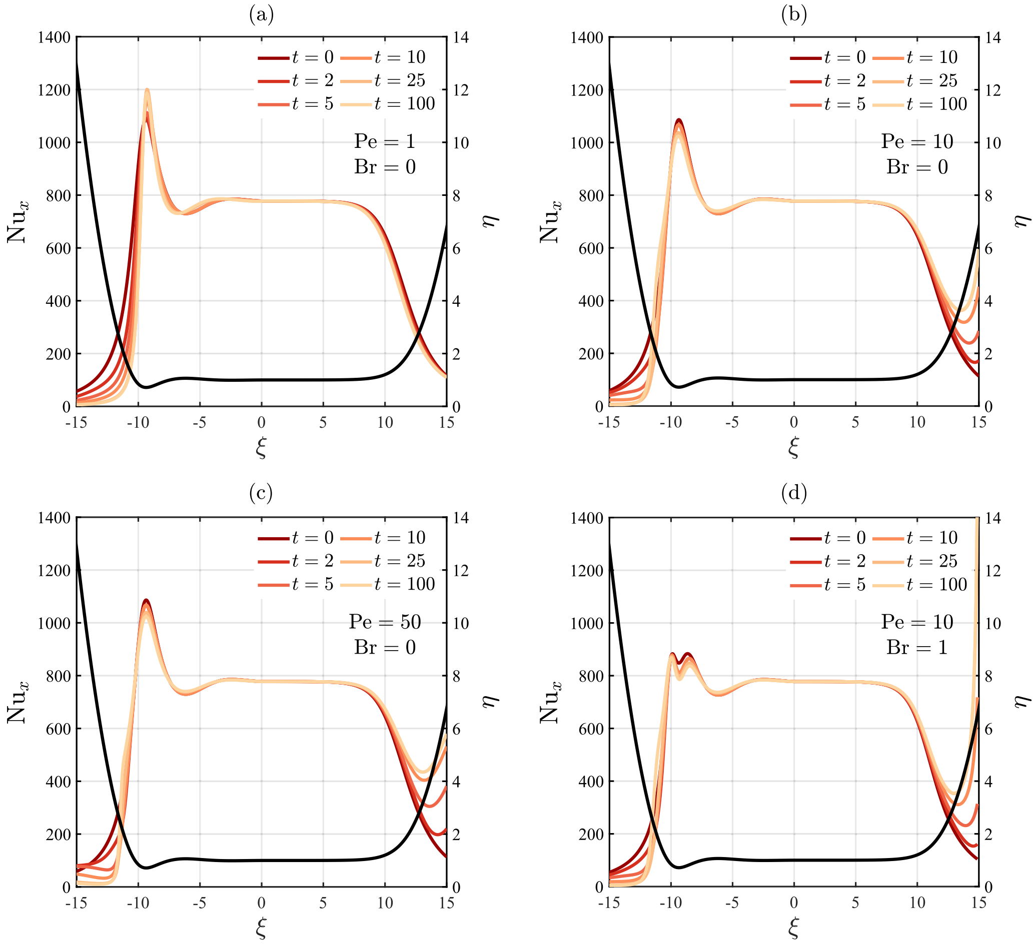

FIG. 5. Impact of the Péclet (Pe) and Brinkman (Br) numbers on the local Nusselt number Nu_x for the cases shown in Fig. 4 (i.e., $\varepsilon = 0.1$, corresponding to $\mathrm{Ca} \approx 3.33 \times 10^{-4}$); right, meniscus profile $\eta(\xi)$.

while the Nusselt number in the uniform-film region is independent of its length l, i.e., $\overline{\mathrm{Nu}}_0 = \mathrm{Nu}_0$. Therefore, we can define the averaged Nusselt number at the film level as

$$\overline{\mathrm{Nu}}(t,\ \mathrm{Pe},\ \mathrm{Br},\ \varepsilon) = \frac{\Delta l_{\mathrm{rear}}\,\overline{\mathrm{Nu}}_{\mathrm{rear}} + l\,\mathrm{Nu}_0 + \Delta l_{\mathrm{front}}\,\overline{\mathrm{Nu}}_{\mathrm{front}}}{\Delta l_{\mathrm{rear}} + l + \Delta l_{\mathrm{front}}}. \tag{48}$$

In Fig. 6, we examine the impact of the Péclet and Brinkman numbers at a fixed capillary number ($\varepsilon = 0.1$) on the time evolution of $\overline{\mathrm{Nu}}$ in the front and in the rear of the bubble. Typically, the averaged Nusselt number increases with time and exhibits an S-shaped evolution at the front, whereas a reversed trend in the rear, see Fig. 6(a). An exception occurs for Pe = 1, where diffusion competes with advection, resulting in a monotonically decreasing profile of the averaged Nusselt number at the front. When the problem is thermally fully developed, $t \gg 0$, in the front, the final $\overline{\mathrm{Nu}}_{\mathrm{front},\,t\to\infty}$ increases with the Péclet number and saturates to a common asymptotic value for Pe = 50 and Pe = 90. At the rear, instead, $\overline{\mathrm{Nu}}_{\mathrm{rear},\,t\to\infty}$ follows a nonmonotonic trend increasing in the following order Pe = (1, 2, 90, 50, 10). Interestingly, at high Péclet numbers (Pe > 10), the average Nusselt number in the rear exhibits an undershoot followed by damped oscillations, reflecting the emergence of transient thermal instabilities before reaching thermally developed

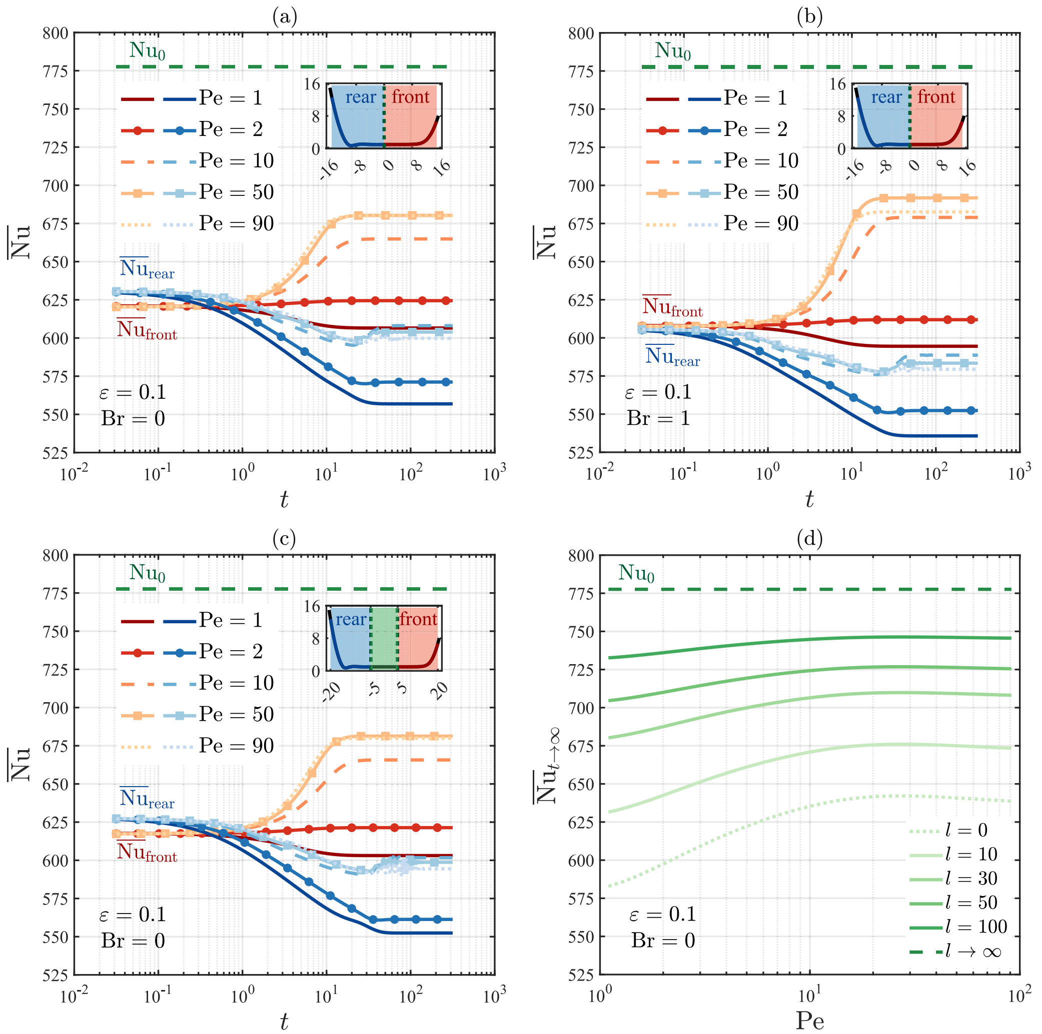

FIG. 6. Impact of the Péclet (Pe) and Brinkman (Br) numbers on the averaged Nusselt numbers for the front ($\overline{\mathrm{Nu}}_{\mathrm{front}}$), rear ($\overline{\mathrm{Nu}}_{\mathrm{rear}}$), and uniform-film ($\mathrm{Nu}_0$) regions, see Eqs. (47) and (45). Time-dependent evolution of the averaged Nusselt numbers at different Péclet numbers for fixed values of flat-film length l and Brinkman number: *(a)* $l = 0$ and $\mathrm{Br} = 0$, *(b)* $l = 0$ and $\mathrm{Br} = 1$, *(c)* $l = 10$ and $\mathrm{Br} = 0$. *(d)* Influence of l on the film-averaged Nusselt number $\overline{\mathrm{Nu}}$, given in Eq. (48), under thermally fully developed conditions. Small-scale parameter: $\varepsilon = 0.1$.

conditions. The effect of viscous dissipation ($\mathrm{Br} = 1$) yields a similar overall trend, as shown in Fig. 6(b). The only difference is that the long-time value in the front increase according to the sequence $\mathrm{Pe} = (1,\ 2,\ 10,\ 90,\ 50)$ rather than monotonically with the Péclet number due to the competing effects of advection and viscous heating.

In Fig. 6(c) we show the impact of a uniform film of 10 dimensionless units in length. The overall behavior is similar to that described in Fig. 6(a) for the case $l = 0$, except for the fact that increasing its length leads to more intense and irregular fluctuations in the averaged Nusselt number in the bubble rear in regimes where advection is dominant. The uniform film length has the strongest impact on the final $\overline{\mathrm{Nu}}_{t\to\infty}$ taken over the entire bubble: as l increases, it converges toward the uniform-film value Nu_0 due to its growing relative weight in the spatial average (48); see Fig. 6(d).

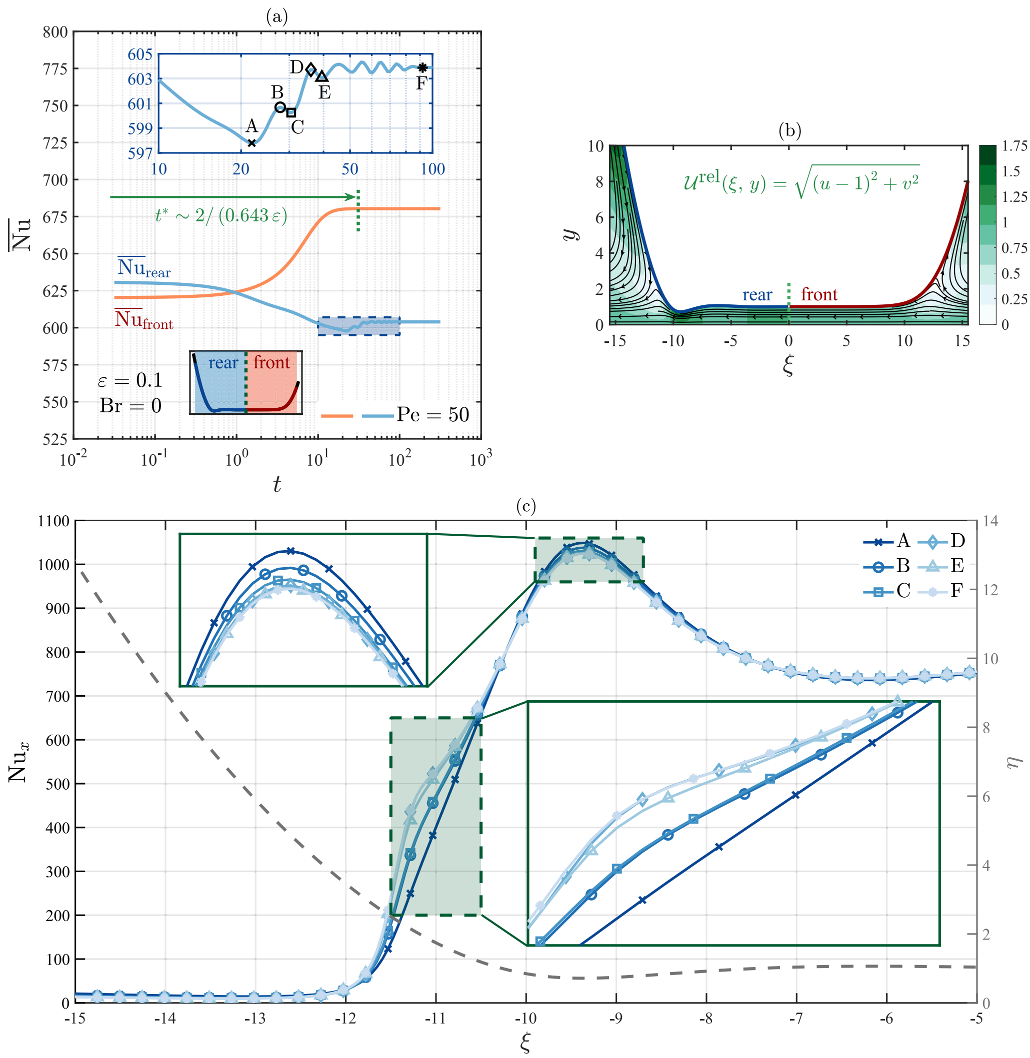

FIG. 7. (a) Temporal evolution of the averaged Nusselt number at the front and rear of the bubble, highlighting six reference points (labeled "A" to "F") illustrating the oscillatory dynamics. (b) Streamlines in the moving reference frame and contours of the relative velocity magnitude $\mathcal{U}^{\mathrm{rel}}$, see Eq. (C1). For the selected time instants, spatial evolution along the rear interface of (c) the local Nusselt number. Small-scale parameter: $\varepsilon = 0.1$.

To better understand the time evolution of the average Nusselt number, we try to illustrate the underlying physical mechanisms in Fig. 7 choosing Pe $= 50$, where the time oscillations in the bubble rear are present. Specifically, in the front, the time required for the Nusselt number to reach its final value is of the order of the time required for a fluid particle initially in contact with the wall to reach the channel centerline and return. This time interval can be estimated as the time required for the bubble to travel a distance equal to the channel diameter, equal to $t^* \sim (2\,R/U_b)(U_b/L) = 2(0.643\,\varepsilon)^{-1}$ in dimensionless terms, see Fig. 7(a). In fact, in the front, clockwise vortices entrain hot fluid into the computational domain, enhancing forced convection and increasing the averaged Nusselt number over time [see the streamlines in a reference frame attached to the bubble in

Fig. 7(b)]. Conversely, at the rear, the vortices advect hot fluid away from the film, leading to a reduction of heat transfer.

The oscillatory behavior of the averaged Nusselt number at the bubble rear—also identified in previous studies (e.g., Refs. [32,78,79])—is linked to the coupling between the interface geometry and the development of flow recirculation in the rear, resulting in intermittent heating and cooling flow patterns [38,80]. To show this, we identify six characteristic time instants ("A" to "F") in Fig. 7(a). Specifically, the temporal fluctuations originate from the flow constriction at the point of minimum film thickness, where a heat pulse forms and remains trapped in the recirculation zone. At the location of the bubble undulations in the rear the effective advection coefficient $u^{\star}$ changes sign, see Fig. 3(a), and the hotspot is advected back and forth. This alters the temperature distribution, progressively reducing the maximum of the local Nusselt number at $\xi \approx -9.5$ and distorting its profile near $\xi \approx -11.5$ [see Fig. 3(c)]. The interplay between peak suppression and hump formation modifies the area under the local Nusselt number, namely, the average Nusselt number over the film length. Over time, diffusion and the heat entering from the wall smooth out the hotspot, as illustrated in the Supplemental Material Movie [81].

V. CONCLUSIONS

In this paper, we developed an asymptotic one-dimensional model to describe forced convection in the liquid film surrounding a single elongated bubble within a horizontal channel subjected to a uniform heat flux. The resulting formulation can be interpreted within an extended Graetz-type framework, where transport under creeping-flow conditions is governed by the competition between advection and diffusion. In the visco-capillary regime—characterized by negligible gravitational and inertial effects—and in the limit of an inviscid, nonconductive gas phase, the mathematical description of the system reduces to a single advection–diffusion-heat-transfer equation, where the dominant thermal transport mechanisms, namely, transverse diffusion and axial advection, are modeled through effective coefficients that depend exclusively on the Péclet and Brinkman numbers, as well as on the geometry of the gas–liquid interface. Interestingly, the resulting diffusion coefficient generalizes the classical Taylor-Aris dispersion to thermal dispersion in a thin film.

We derived a closed-form expression for the Nusselt number, elucidating how film-driven flow confinement enhances heat transfer compared to the single-phase regime. In the uniform-film region, the local Nusselt number remains uniform and scales inversely with the capillary number following a 2/3 power-law, highlighting the impact of phase topology on heat removal efficiency. Additionally, we clarified the role of recirculation patterns emerging at the front and rear menisci in shaping the overall thermal response of the film under advection-dominated conditions. We demonstrated that the formation of hotspots at the point of minimum film thickness—resulting from the interplay between purely diffusive transport in the uniform-film region and the flow constriction in the bubble rear—gives rise to an oscillatory thermal dynamics of the averaged Nusselt number. Our analysis is complemented by the identification of the model's applicability region, where upscaling remains a physically consistent approach.

Future work may explore the extension of this framework to regimes with larger capillary numbers and with fluid evaporation/condensation. This would enable the investigation of thermal interactions between consecutive slugs in bubble-train flows, shedding light on more complex flow patterns and their influence on the overall heat-transfer performance in heat-transfer applications.

ACKNOWLEDGMENTS

This study has received funding from the European Union "NextGenerationEU," Ministero dell'Università e della Ricerca (MUR) "Italiadomani" Piano Nazionale di Ripresa e Resilienza (PNRR), Mission 4, Research Project PRIN 2022 "Predictive forecasting and risk assessment for CO_2 transport in pipelines," MUR code: 20229JPN53; CUP Master code: J53D23002000006; CUP code: D53D23003250006.

The authors report no conflict of interest.

DATA AVAILABILITY

The data that support the findings of this article are not publicly available. The data are available from the authors upon reasonable request.

APPENDIX A: VALIDITY OF BRETHERTON THEORY

By applying the lubrication approximation to the Navier-Stokes equations over a characteristic length $L = h_\infty(3\,\mathrm{Ca})^{-1/3}$ and retaining only the leading-order terms, Bretherton [3] derived the equation (1) for the dimensionless profile of the dynamic menisci. This formulation is valid provided that $\varepsilon = (3\,\mathrm{Ca})^{1/3} \ll 1$ and $\mathrm{Re} \ll 1$. Consequently, the Bretherton [3] theory is no longer applicable to bubbles exhibiting a long transition region with a sharp tip, as well as to flows with nonnegligible inertia [56]. Several extensions have been proposed to relax these limitations. In particular, Aussillous and Quéré [82] and Klaseboer *et al.* [83] introduced a saturation term in the asymptotic matching condition (3), allowing the model to be applicable at finite capillary numbers so that it describes the deposition of thicker films. Later on, de Ryck [84] and Magnini *et al.* [85] developed a more complete analytical framework to include the full expression of the film curvature in a circular tube and retain all terms of order $\mathcal{O}(\varepsilon)$, accounting also for finite inertia as long as $\varepsilon^2 \ll 1$. While these models recover the model of Bretherton [3] at low Ca, they exhibit deviations at higher values of the capillary number. The comparison among these models is summarized in Fig. 8. Figure 8(a) shows the predicted dimensionless film thickness, highlighting that the classical $2/3$ scaling holds only in the low-Ca limit. In terms of absolute relative error, Fig. 8(b), the Bretherton asymptotic law (3) remains within 2% for $\mathrm{Ca} < 5 \times 10^{-4}$ with respect to the model proposed by de Ryck [84] and Magnini *et al.* [85]. Note that, the latter models provides a more accurate reconstruction of the film profile by accounting for the full expression of the interface curvature $\hat{\kappa}$ (see Eq. (20) in Magnini *et al.* [85]).

In this work, we limit our interest in the low-Ca regime choosing $\varepsilon = 0.1$, corresponding to $\mathrm{Ca} \approx 3.33 \times 10^{-4}$. Thus, the error in predicting the film thickness using the leading-order Bretherton theory instead of the one by de Ryck [84] is still small [around 1.4% in Fig. 8(b)]. As shown in Fig. 8(c), the relative error on the film profile $\eta(\xi)$ between the Bretherton [3] model and that of de Ryck [84] is below 2% for $\eta \lesssim 15$ (highlighted by the circular marker), which corresponds to a film thickness of approximately 10% of the channel radius; in this work we compute the film profile approximately up to that point. Note that the the model of de Ryck [84] and Magnini *et al.* [85] enables the matching between the dynamic film region and a static spherical cap, as shown in Fig. 8(d), at the point (highlighted by the asterisk) where the axial and transverse components of the curvature coincide. This extends the film profile closer to the tube axis as the capillary number increases.

It is also worth mentioning that the Bretherton theory breaks down at ultra-low capillary numbers where long-range intermolecular forces, such as van der Waals interactions, must be taken into account to accurately describe the thin-film dynamics [86–89]. Therefore, the present analysis is restricted to regimes where the capillary number is sufficiently small that the effect of full description of the film curvature with respect to the Bretherton theory remains small and, at the same time, the capillary number is still above the threshold below which the disjoining pressure plays a role.

APPENDIX B: EQUIVALENCE OF THE PLANAR AND RADIAL COORDINATES IN THE LOW Ca LIMIT

In this Appendix we show that, in the $\mathrm{Ca} \ll 1$ limit, the planar and the axisymmetric configurations are asymptotically equivalent as in Ref. [3]. Specifically, recalling that the transverse and the

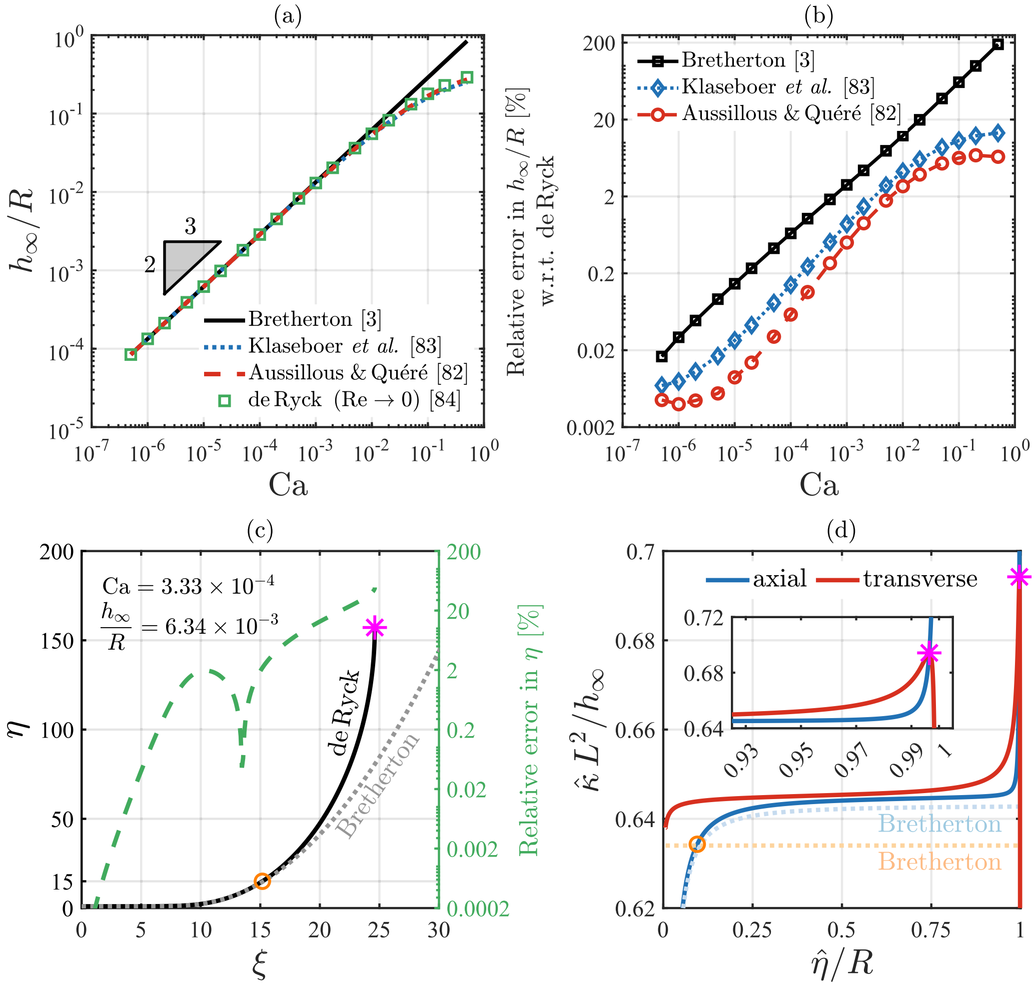

FIG. 8. (a) Dimensionless film thickness predicted by different models and (b) corresponding absolute relative error (in percent) with respect to the inertialess limit of the model of de Ryck [84], as a function of the capillary number. For $\varepsilon = 0.1$, (c) comparison of the front meniscus profiles predicted by the Bretherton [3] model and by the model of de Ryck [84]; right axis: absolute relative error (in percent); (d) axial and transverse components of the dimensionless interface curvature as a function of the transverse location: model of de Ryck [84] (solid lines) and Bretherton model (dashed lines). Asterisk: point corresponding to the matching condition. Circular marker: $\eta = 15$.

radial coordinates are related via $\hat{y} = R - \hat{r}$ (see Fig. 1) and using Eq. (3) we obtain

$$\frac{\hat{y}}{h_\infty} = \frac{1 - \hat{r}/R}{0.643(3\,\mathrm{Ca})^{2/3}}, \tag{B1}$$

that maps the thin layer onto an $\mathcal{O}(1)$ interval [90,91]. Then, applying the chain rule we see that the the differential operators in cylindrical coordinates reduce to their planar counterparts up to

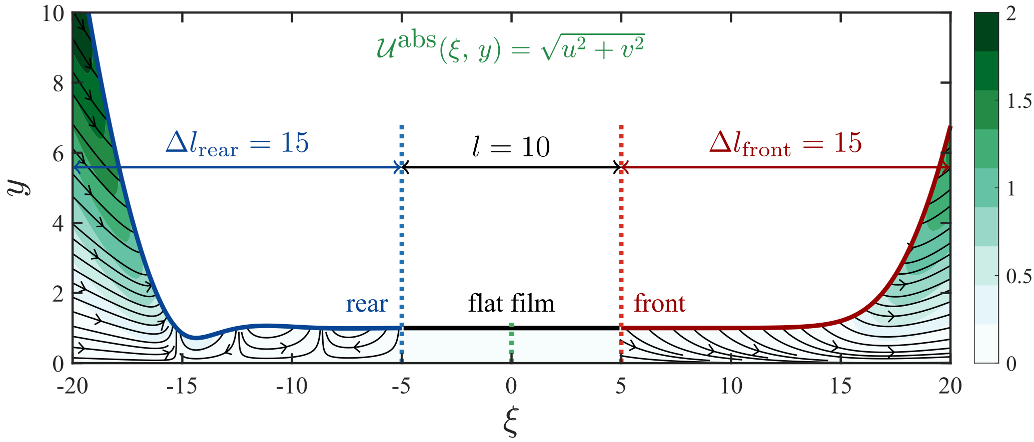

FIG. 9. Streamlines in the laboratory reference frame and contours of the absolute velocity magnitude $\mathcal{U}^{\rm abs}$, see Eq. (C1).

higher-order corrections ($y = \hat{y}/h_\infty$ and $r = \hat{r}/R$):

$$\frac{1}{r}\,\partial_r(r\,\star) = -\frac{\partial_y\star}{0.643(3\,\mathrm{Ca})^{2/3}} + \frac{\star}{1-0.643(3\,\mathrm{Ca})^{2/3}\,y} \approx -\frac{\partial_y\star}{0.643(3\,\mathrm{Ca})^{2/3}}, \tag{B2a}$$

$$\frac{1}{r}\,\partial_r(r\,\partial_r\,\star) = \frac{1}{0.643^2(3\,\mathrm{Ca})^{4/3}}\left(\partial_{yy}\,\star - \frac{0.643(3\,\mathrm{Ca})^{2/3}}{1-0.643(3\,\mathrm{Ca})^{2/3}\,y}\,\partial_y\star\right) \approx \frac{\partial_{yy}\star}{0.643^2(3\,\mathrm{Ca})^{4/3}}. \tag{B2b}$$

APPENDIX C: VELOCITY PROFILE IN THE THIN FILM

The velocity profile in the thin film is obtained following the classical Landau-Levich-Derjaguin-Bretherton theory, by means of the lubrication approximation, as shown in Ref. [3]. Specifically, the axial velocity u follows from the incompressible Stokes equation for a Newtonian free-surface film, while the transverse component v is obtained via the continuity equation [45], yielding the following dimensionless velocity components

$$u(\eta,\,y) = \frac{3\,y(\eta-1)(2\,\eta-y)}{2\,\eta^3}, \qquad v(\eta,\,y) = \frac{y^2[(3-2\,\eta)y - 3\,\eta(2-\eta)]}{2\,\eta^4}\,\frac{\mathrm{d}\eta}{\mathrm{d}\xi}. \tag{C1}$$

These expressions fix a typo with respect to Eqs. (A7) and (A8) in Picchi and Poesio [45], where a prefactor 3 [consistent with the axial stretching embedded in the definition of the small-scale parameter (2)] is missing. Figure 9 provides the streamline representation of the velocity field in the laboratory reference frame. Given the velocity profiles, the viscous dissipation function is computed analytically as

$$\Phi(\eta,\,y) = 2\,\varepsilon^2\left[\left(\frac{\partial\,u}{\partial\xi}\right)^2 + \left(\frac{\partial\,v}{\partial y}\right)^2\right] + \left(\frac{\partial\,u}{\partial y} + \varepsilon^2\frac{\partial\,v}{\partial\xi}\right)^2 = \left[\frac{3(\eta-1)(\eta-y)}{\eta^3}\right]^2 + \mathcal{O}(\varepsilon^2). \tag{C2}$$

APPENDIX D: ACCURACY OF THE EFFECTIVE MODEL

The one-dimensional effective model (34) is validated with the depth-averaged temperature [through the operator (20)] of the two-dimensional solution $\theta_{2\mathrm{D}}$ of the full energy balance equation (10). The latter is computed using the finite element method (FEM) discretization scheme, implemented via MATLAB's built-in Partial Differential Equation Toolbox, PDETOOL [92]. The

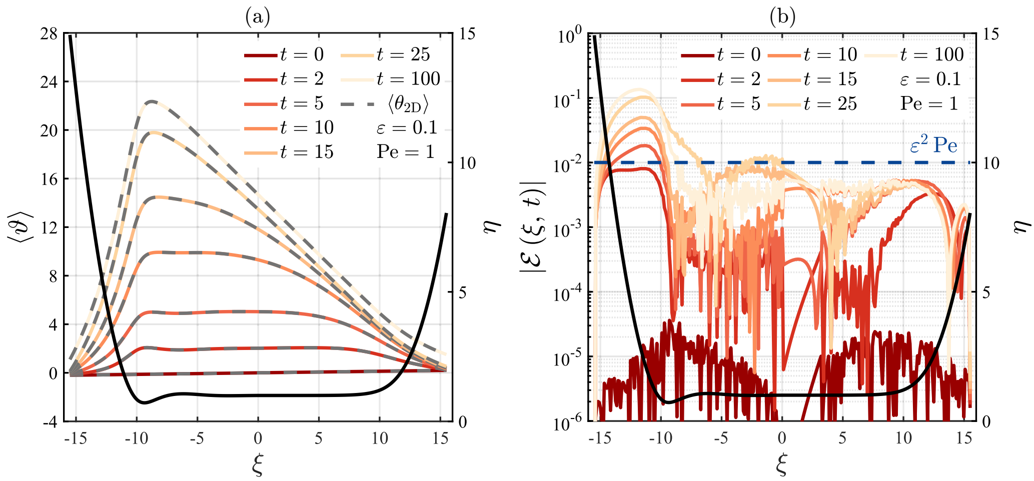

FIG. 10. (a) Time evolution of the average film temperature $\langle\vartheta\rangle$ along a cylindrical tube ($m = 1$) under uniform heating ($\nu = -1$), obtained from the effective model (34) (solid lines) and the 2D full problem (10) (dashed gray lines: θ_{2D}) for Pe = 1 and Br = 0. (b) Absolute error $|\mathcal{E}(\xi, t)| = |\langle\theta_{2D}\rangle - \langle\vartheta\rangle|$ corresponding to each pair of temperature profiles. The dashed horizontal blue line represents the theoretical error bound prescribed by homogenization with $\varepsilon = 0.1$. Right, meniscus profile $\eta(\xi)$ with $l = 0$.

computational domain is delimited by four sides: the Dirichlet-type conditions (39) are imposed on the left and right boundaries; the Neumann condition (13) prescribing a uniform heat flux is applied at the bottom wall; and the adiabatic condition—corresponding to Eq. (15) in the limit of $\mathcal{K} \to 0$—is enforced on each mesh element of the bubble fluid interface obtained solving Eq. (1) and discretizing it according to the mesh elements. The initial temperature field ($t \to 0$) is set to the linear profile (39), while the problem is solved in a reference frame attached to the bubble. The liquid film is represented using an adaptive triangular mesh composed of quadratic elements—with nodes at corners and edge centers—characterized by a maximum element height of 0.025 and a growth rate of 2, ensuring adequate resolution near the interface. A polygonal approximation is used to reconstruct the front and rear film domains, based on 301 uniformly spaced points along the longitudinal direction. To interpolate data from mesh nodes onto a rectangular Cartesian grid and perform transverse averaging, a uniform spatial resolution of $\Delta y \approx 2.5 \times 10^{-4}$ is used over the interval $[0; \max_\xi \eta]$. Consistent with our analysis in Sec. IV, the numerical simulations are performed at a fixed capillary number (i.e., $\varepsilon = 0.1$) and they are stopped when the temperature field reaches fully thermal development conditions, corresponding to a dimensionless time $t \sim 100$.

To evaluate the accuracy of the effective model, we introduce the absolute error $\mathcal{E}(\xi, t) \equiv \langle\theta_{2D}\rangle - \langle\vartheta\rangle$ between the averaged fully resolved solution and its approximation obtained via the asymptotics. This metric is widely adopted to estimate the error introduced by the asymptotic expansions and unresolved high-order terms [66,93].

Figure 10(a) compares the spatial evolution of the averaged fully resolved solution and its approximation obtained via two-scale expansions at fixed time instants choosing the lowest admissible Péclet number, Pe = 1, which gives the most stringent tolerance criteria. In fact, the upscaled solution is predictive of the small-scale behavior only if the absolute error remains bounded by the expansion parameter, i.e., $|\mathcal{E}| \lesssim \varepsilon^2$ Pe. As shown in panel (*a*), the averaged temperature profiles overlap at each time considered, indicating an excellent agreement between the full and the approximated solution. In panel (*b*), we analyze the spatial distribution of the absolute error along the bubble profile. The error remains bounded by ε^2 Pe over most of the domain except for a small region in the bubble's rear where, at sufficiently high times, it locally exceeds this theoretical threshold

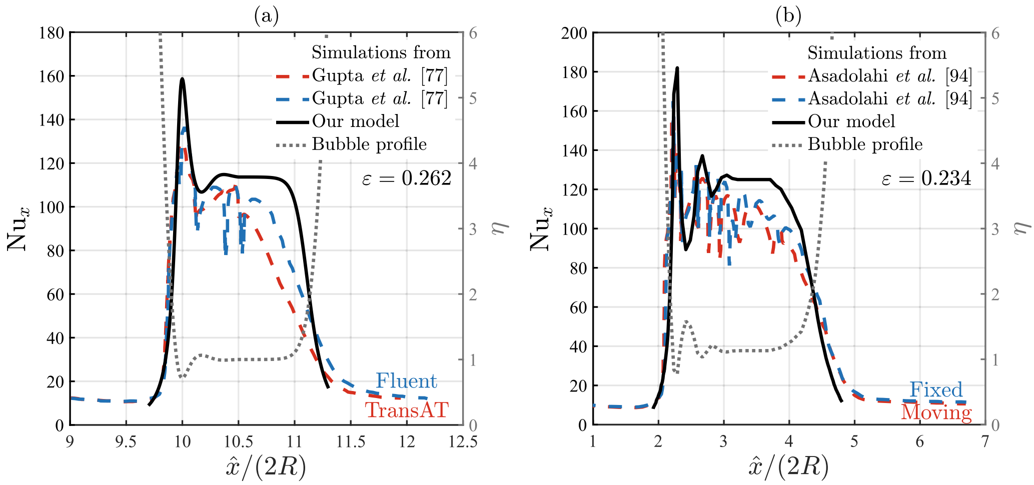

FIG. 11. Comparison between the spatial evolution of the local Nusselt number Nu_x predicted by the upscaled model (with $m = 1$) in the limit $\Gamma \to 0$ (continuous black line)—see Eqs. (45) and (46)—and available results from numerical simulations of an elongated bubble in a horizontal capillary under iso-flux boundary conditions: (a) Gupta *et al.* [77], (b) Asadolahi *et al.* [94] (blue and red dashed lines); right, meniscus profile $\eta(\xi)$ (dotted gray line). Here, $\hat{x}$ denotes the dimensional axial coordinate relative to the laboratory reference frame, consistent with the cited works.

($-15 \lesssim \xi \lesssim -10$). This is attributed to a localized steepening of the temperature profile that makes the first derivative of the averaged temperature greater than the unity, i.e., $|\partial\langle\vartheta\rangle/\partial\xi| \gtrsim \mathcal{O}(1)$, amplifying the contribution of higher-order corrections in Eq. (29). We recall that an underlying hypothesis of methods based on two-scale asymptotics is that, after normalization, the derivatives remain of order one, but, as in this case, there may exist regions of the domain where this condition is not met. Despite this, the absolute error remains small, confirming the robustness and reliability of the approach, as shown in Fig. 10(a).

APPENDIX E: COMPARISON WITH EXISTING LITERATURE

In Fig. 11, we compare the local Nusselt number predicted by the scaling law (45) derived from the effective model (34) with two numerical studies from the literature, detailed in Table II. Unfortunately, a survey of the literature did not reveal experimental or numerical data for the heat transfer problem within the applicability region of the model expressed by Eq. (35), particularly in the limit of $\mathrm{Ca} \to 0$ and $\mathrm{Re} \to 0$. Specifically, in both cases, $\mathrm{Ca} = \mathcal{O}(10^{-3})$, while the Reynolds number is finite, $\mathrm{Re} = \mathcal{O}(10^2)$, for which inertial effects cannot be ignored, especially in the undulations of the bubble rear [84,85]. Also the Péclet numbers slightly exceed the theoretical bound expressed by Eq. (35), implying that, since the inequalities given by Eq. (35) are not met, the rigorous thermal decoupling between the transverse and the axial scales cannot be guaranteed [95]. Nevertheless, it is worth recalling that those constraints provide only sufficient but not necessary conditions, and are, in some, cases even too restrictive [62,96,97]. Therefore, we compare the numerical data of Gupta *et al.* [77] and Asadolahi *et al.* [94] with the local Nusselt number obtained with our model neglecting (i) the viscous dissipation, since the Brinkman number is of order $<10^{-3}$, see Table II; and (ii) the contribution of the axial temperature gradient, that is not given in those two works. This corresponds to the limit $\lim_{\Gamma\to 0} \mathrm{Nu}_x$ (with $m = 1$), see Eqs. (45) and (46).

Figure 11(a) shows the comparison with Gupta *et al.* [77] where the elongated bubble is investigated using both the level-set and volume-of-fluid implemented through the *TransAT* (dashed red line) and *ANSYS Fluent* (dashed blue line) codes, respectively. Note that the discrepancies between

TABLE II. Summary of simulation parameters adopted in two numerical studies on heat transfer in nonboiling gas-liquid Taylor flow within horizontal circular ($m = 1$) microchannels subject to iso-flux heating ($\nu = -1$) boundary condition at the wall; see Fig. 11.

Parameter [unit of measurement]	Symbol	Gupta *et al.* [77]	Asadolahi *et al.* [94]
Reference frame		fixed	fixed and comoving
Tube radius [m]	R	2.5×10^{-4}	1×10^{-3}
Specific wall heat flux [W/ m^2]	$\lvert q_w'' \rvert$	3.20×10^{4}	3.20×10^{4}
Gas/liquid		air/water	nitrogen/water
Liquid dynamic viscosity [Pas]	μ_f	8.90×10^{-4}	8.90×10^{-4}
Liquid thermal conductivity [W m^{-1} K^{-1}]	κ_f	0.6	0.6
Liquid density [kgm^{-3}]	ρ_f	997	997
Surface tension [Nm^{-1}]	σ	0.072	0.072
Gas-to-liquid viscosity ratio		2.06×10^{-2}	2.36×10^{-2}
Gas-to-liquid thermal conductivity ratio	$\mathcal{K}$	4.03×10^{-2}	4.03×10^{-2}
Uniform film thickness [m]	h_∞	1.10×10^{-5}	4.10×10^{-5}
Scale parameter	ε	0.262	0.234
Bubble mean velocity [ms^{-1}]	U_b	0.483	0.348
Interfacial length [m]	L	4.21×10^{-5}	1.75×10^{-4}
Capillary number	$\mathrm{Ca} = \mu_f U_b/\sigma$	5.97×10^{-3}	4.30×10^{-3}
Reynolds number	$\mathrm{Re} = \rho_f U_b R/\mu_f$	135	390
Weber number	$\mathrm{We} = \mathrm{Ca}\,\mathrm{Re}$	0.80	1.67
Bond number	$\mathrm{Bo} = \rho_f g R^2/\sigma$	8.50×10^{-3}	1.36×10^{-1}
Péclet number	$\mathrm{Pe} = L U_b/\alpha_f$	141	422
Brinkman number	$\mathrm{Br} = \dfrac{\mu_f U_b^2}{\lvert q_w'' \rvert h_\infty}$	5.89×10^{-4}	8.19×10^{-5}
$-\log_\varepsilon \mathrm{Pe}$	p	3.69	4.17
$+\log_\varepsilon \mathrm{Br}$	b	5.55	6.49
$+\log_\varepsilon \mathcal{K}$	k	2.39	2.21

these two numerical models are caused by differences in the description of the curvature of the meniscus, which is reconstructed in one case and explicitly tracked in the other. Since the gas-liquid interface is not reported in Fig. 7 of Gupta *et al.* [77], we reproduce the bubble profile (right ordinate) using the Bretherton equation (1), adjusting its length, and translating it along the axial coordinate to fit with the simulated bubble. Overall, our model exhibits good qualitative and quantitative agreement with both the numerical simulations, except for the undulating evolution of the Nusselt number in the bubble's rear. Those inertia-driven undulations are typical of high-Reynolds-number regimes [98], and are not captured by Bretherton similarity equation.

Figure 11(b) shows the local Nusselt number data from Asadolahi *et al.* [94] obtained using *ANSYS Fluent* for a unit cell moving with the bubble speed (dashed red line) and with respect to the laboratory reference frame (dashed blue line). Since Fig. 12 of Asadolahi *et al.* [94] reports the computed bubble profile (right ordinate), we use that profile to compute Nu_x instead of that derived from Bretherton equation (1). Also in this case, the agreement between the scaling law (45) and the simulations is quite satisfactory, confirming the primary role of the film thickness in driving the local evolution of the Nusselt number, similarly to observations reported in earlier works on core-annular flows [49].

Thanks to its capability of accounting for the thin-film profile, we believe that the scaling law (45) has the potential of being integrated in widely used mechanistic models for trains of elongated bubbles [9,16,17,35,99].

APPENDIX F: OTHER DEFINITIONS OF THE AVERAGE NUSSELT NUMBER

Since its definition is not unique, here, we discuss other definitions of the averaged Nusselt number that differ from the one obtained by averaging the local Nusselt number given in Eq. (48). Although, according to Newton's law of cooling, the local convective heat transfer coefficient at a solid boundary is defined as the ratio between the heat flux per unit area and a reference temperature difference, its spatial average varies from case to case.

For example, in the case of external flows (e.g., laminar and incompressible thermal boundary layer over a flat plate), such temperature difference is typically taken between the wall and the free-stream temperature. Then, the average heat transfer coefficient is defined as the mean flux normalized by the fixed temperature difference (in the case of isothermal wall), or as the flux normalized by the mean temperature difference (in the uniform-flux case). In both cases, the averaged Nusselt number is not obtained by averaging the local Nusselt number [76,100].

In contrast, in internal convection problems, the reference temperature difference is not uniquely defined and varies across experimental and numerical studies [101]. This ambiguity leads to different definitions of the Nusselt number, particularly in problems with nonisothermal boundaries [102]. The most common approach is to use the temperature difference between the tube wall and a the enthalpy-weighted average temperature, commonly known as the bulk or mixing-cup temperature [74,103]; see Eq. (41). Other definitions of temperature difference (e.g., wall-to-bulk, wall-to-inlet, mean wall-to-inlet, etc.) are usually guided by the application and the imposed boundary condition [28]. For example, in single-phase channel flow under uniform flux conditions the local Nusselt number varies only in the thermal entrance region, making the definition of the averaged Nusselt number as the integral of the local one not relevant outside the entrance region. In this case, in fact, an alternative formulation of the mean Nusselt number based on a domain-averaged temperature difference is usually adopted. In other words, instead of averaging the local Nusselt number over the spatial domain as in Eq. (48), the strategy is to divide the flux by the difference between the domain-averaged wall temperature and the domain-averaged bulk temperature.

This idea has been borrowed from many works in the context of slug and Taylor flows, where researchers have been using averaged wall and bulk temperatures [104,105], to define the averaged Nusselt number over a representative unit cell (e.g., Refs. [38,77,80,94]). Specifically, the Nusselt number obtained from the averaged temperature difference reads

$$\widetilde{\mathrm{Nu}} = -\frac{2(2-m)}{0.643(3\,\mathrm{Ca})^{2/3}}\,\frac{\nu}{\overline{\vartheta_w^{(1)}} - \overline{\vartheta_b^{(1)}}}, \quad \text{with} \quad \begin{cases} \overline{\vartheta_w^{(1)}} \equiv \frac{1}{\ell}\int_\ell \vartheta_w^{(1)}\,\mathrm{d}\xi, \\ \overline{\vartheta_b^{(1)}} \equiv \frac{\int_\ell\int_0^\eta u\,\vartheta_b^{(1)}\mathrm{d}y\,\mathrm{d}\xi}{\int_\ell\int_0^\eta u\,\mathrm{d}y\,\mathrm{d}\xi}, \end{cases} \tag{F1}$$

where, in analogy with Eq. (47), the overline denotes a domain average performed over a longitudinal distance $\ell = \Delta l_{\mathrm{rear}} + l + \Delta l_{\mathrm{front}}$. The domain-averaged first-order corrections to the wall and bulk temperatures are shown in Fig. 12(a) and their final values vary nonmonotonically with the Péclet number, increasing for the bulk and decreasing for the wall in the sequence $\mathrm{Pe} = (10,\ 2,\ 1,\ 50,\ 90)$. Accordingly, the $\widetilde{\mathrm{Nu}}$ normalized by the single-phase reference value for a cylindrical tube $\mathrm{Nu}_{\mathrm{sp}} = 48/11 \approx 4.36$ is shown in Fig. 12(b). The Nusselt number decreases monotonically in the diffusion-dominated regimes, while for $\mathrm{Pe} > 50$ it displays a nonmonotonic trend with an intermediate maximum before reaching thermally fully developed conditions. Specifically, the final value indicates a heat-transfer enhancement ranging from 6 to 16 times with respect to single-phase flow.

An alternative formulation has been proposed by Ref. [106] as a time-averaged local Nusselt number based on wall and bulk temperatures averaged over the recirculation period, motivated by the periodicity of Taylor flow in a reference frame attached to the bubble. This definition has been reported to facilitate the comparison between numerical simulations and experimental data since it is easier to measure averaged quantities along a channel segment than knowing the local

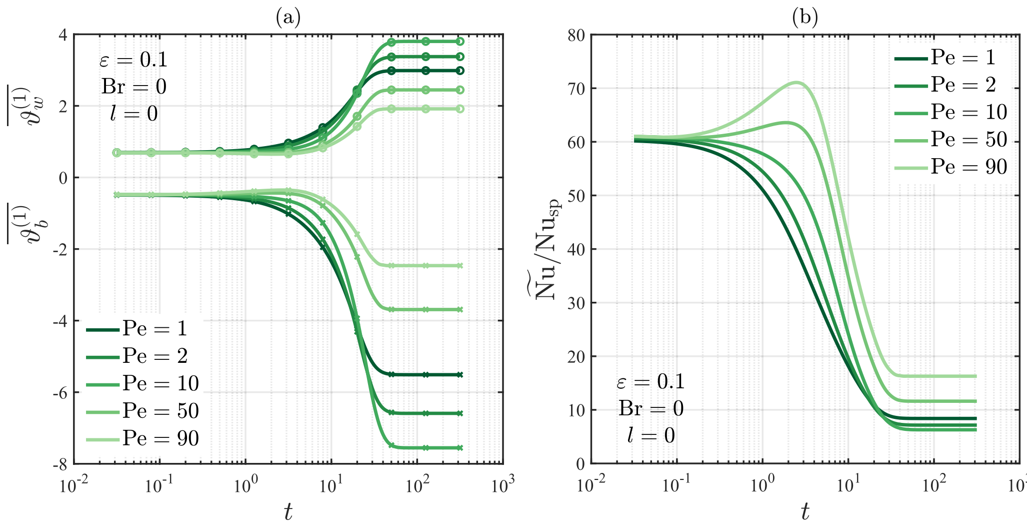

FIG. 12. (a) Time evolution of the domain-averaged first-order corrections to the wall ("w") and bulk ("b") temperatures, and (b) averaged Nusselt number $\widetilde{\mathrm{Nu}}$—see Eq. (F1)—relative to the single-phase value $\mathrm{Nu_{sp}} = 48/11$ in a cylindrical tube ($m = 1$) under uniform flux heating ($\nu = -1$), for different values of the Péclet number Pe, neglecting the impact of viscous dissipation ($\mathrm{Br} = 0$). The domain-average is performed over a distance $\ell = \Delta l_{\mathrm{front}} + \Delta l_{\mathrm{rear}} = 30$, with a negligible uniform film region ($l = 0$). Small-scale parameter: $\varepsilon = 0.1$.

wall temperature field [107]. It is worth mentioning that the detailed analysis of these alternative formulations of the Nusselt number falls outside the scope of our work.

[1] P. Angeli and A. Gavriilidis, Hydrodynamics of Taylor flow in small channels: A review, Proc. Inst. Mech. Eng., Part C **222**, 737 (2008).

[2] G. I. Taylor, Deposition of a viscous fluid on the wall of a tube, J. Fluid Mech. **10**, 161 (1961).

[3] F. P. Bretherton, The motion of long bubbles in tubes, J. Fluid Mech. **10**, 166 (1961).

[4] P. Griffith and G. B. Wallis, Two-phase slug flow, J. Heat Transfer **83**, 307 (1961).

[5] R. A. S. Brown, The mechanics of large gas bubbles in tubes: I. Bubble velocities in stagnant liquids, Can. J. Chem. Eng. **43**, 217 (1965).

[6] R. M. Davies and G. I. Taylor, The mechanics of large bubbles rising through extended liquids and through liquids in tubes, Proc. R. Soc. London A **200**, 375 (1950).

[7] R. Gupta, S. S. Y. Leung, R. Manica, D. F. Fletcher, and B. S. Haynes, Hydrodynamics of liquid-liquid Taylor flow in microchannels, Chem. Eng. Sci. **92**, 180 (2013).

[8] R. Abiev, Analysis of hydrodynamics and mass transfer of gas-liquid and liquid-liquid Taylor flows in microchannels: Theoretical approach and experimental proofs, in *Process Analysis, Design, and Intensification in Microfluidics and Chemical Engineering* (IGI Global, Hershey, PA, 2019), pp. 1–49.

[9] X. Zhang and V. S. Nikolayev, Physics and modeling of liquid films in pulsating heat pipes, Phys. Rev. Fluids **8**, 084002 (2023).

[10] M. Abela, M. Mameli, S. Filippeschi, and V. S. Nikolayev, Experimental and numerical studies of the pulsating heat pipe stopover regime, Int. J. Heat Mass Transf. **247**, 127102 (2025).

[11] S. S. Mehendale, A. M. Jacobi, and R. K. Shah, Fluid flow and heat transfer at micro- and meso-scales with application to heat exchanger design, Appl. Mech. Rev. **53**, 175 (2000).

[12] J. R. Thome, Boiling in microchannels: A review of experiment and theory, Int. J. Heat Fluid Flow **25**, 128 (2004).

[13] M. B. Darshan, M. Magnini, and O. K. Matar, Numerical modelling of flow boiling inside microchannels: A critical review of methods and applications, Appl. Therm. Eng. **257**, 124464 (2024).

[14] I. Mudawar and M. B. Bowers, Ultra-high critical heat flux (CHF) for subcooled water flow boiling—I: CHF data and parametric effects for small diameter tubes, Int. J. Heat Mass Transf. **42**, 1405 (1999).

[15] G. Wang, P. Cheng, and A. E. Bergles, Effects of inlet/outlet configurations on flow boiling instability in parallel microchannels, Int. J. Heat Mass Transf. **51**, 2267 (2008).

[16] J. R. Thome, V. Dupont, and A. M. Jacobi, Heat transfer model for evaporation in microchannels. Part I: Presentation of the model, Int. J. Heat Mass Transf. **47**, 3375 (2004).

[17] V. Dupont, J. R. Thome, and A. M. Jacobi, Heat transfer model for evaporation in microchannels. Part II: Comparison with the database, Int. J. Heat Mass Transf. **47**, 3387 (2004).

[18] S. Szczukiewicz, M. Magnini, and J. R. Thome, Proposed models, ongoing experiments, and latest numerical simulations of microchannel two-phase flow boiling, Int. J. Multiphase Flow **59**, 84 (2014).

[19] M. Magnini, B. Pulvirenti, and J. R. Thome, Numerical investigation of hydrodynamics and heat transfer of elongated bubbles during flow boiling in a microchannel, Int. J. Heat Mass Transf. **59**, 451 (2013).

[20] F. Municchi, I. El Mellas, O. K. Matar, and M. Magnini, Conjugate heat transfer effects on flow boiling in microchannels, Int. J. Heat Mass Transf. **195**, 123166 (2022).

[21] X. Zhang and V. S. Nikolayev, Dewetting acceleration by evaporation, J. Fluid Mech. **948**, A49 (2022).

[22] C. Tecchio, X. Zhang, B. Cariteau, G. Zalczer, P. Roca i Cabarrocas, P. Bulkin, J. Charliac, S. Vassant, and V. S. Nikolayev, Microlayer in nucleate boiling seen as Landau–Levich film with dewetting and evaporation, J. Fluid Mech. **989**, A4 (2024).

[23] X. Zhang, I. El Mellas, and M. Magnini, Predicting initial microlayer thickness in nucleate boiling using Landau-Levich theory, J. Fluid Mech. **997**, A44 (2024).

[24] X. Zhang, I. El Mellas, N. Andreini, and M. Magnini, The microlayer and force balance of bubbles growing on solid in nucleate boiling, Int. J. Multiphase Flow **183**, 105049 (2025).

[25] A. Bar-Cohen, M. Arik, and M. Ohadi, Direct liquid cooling of high flux micro and nano electronic components, Proc. IEEE **94**, 1549 (2006).

[26] T. Bandara, N.-T. Nguyen, and G. Rosengarten, Slug flow heat transfer without phase change in microchannels: A review, Chem. Eng. Sci. **126**, 283 (2015).

[27] R. Gupta, D. F. Fletcher, and B. S. Haynes, Taylor flow in microchannels: A review of experimental and computational work, J. Comput. Multiphase Flows **2**, 1 (2010).

[28] Y. S. Muzychka, E. J. Walsh, and P. Walsh, Heat transfer enhancement using laminar gas-liquid segmented plug flows, J. Heat Transfer **133**, 041902 (2011).

[29] V. Talimi, Y. S. Muzychka, and S. Kocabiyik, Numerical simulation of the pressure drop and heat transfer of two phase slug flows in microtubes using moving frame of reference technique, Int. J. Heat Mass Transf. **55**, 6463 (2012).

[30] A. Etminan and Y. S. Muzychka, Effects of flow characteristics on the heat transfer mechanism in Taylor flow, Int. J. Heat Mass Transf. **219**, 124917 (2024).

[31] G. A. Hughmark, Holdup and heat transfer in horizontal slug gas-liquid flow, Chem. Eng. Sci. **20**, 1007 (1965).

[32] P. A. Walsh, E. J. Walsh, and Y. S. Muzychka, Heat transfer model for gas-liquid slug flows under constant flux, Int. J. Heat Mass Transf. **53**, 3193 (2010).

[33] S. S. Y. Leung, Y. Liu, D. F. Fletcher, and B. S. Haynes, Heat transfer in well-characterised Taylor flow, Chem. Eng. Sci. **65**, 6379 (2010).

[34] M. T. Kreutzer, P. Du, J. J. Heiszwolf, F. Kapteijn, and J. A. Moulijn, Mass transfer characteristics of three-phase monolith reactors, Chem. Eng. Sci. **56**, 6015 (2001).

[35] Z. Dai, Z. Guo, D. F. Fletcher, and B. S. Haynes, Taylor flow heat transfer in microchannels—Unification of liquid-liquid and gas-liquid results, Chem. Eng. Sci. **138**, 140 (2015).

[36] L. Graetz, Ueber die Wärmeleitungsfähigkeit von Flüssigkeiten (On the thermal conductivity of liquids), Ann. Phys. **254**, 79 (1882).

[37] A. Lévêque, *Les Lois de la Transmission de Chaleur Par Convection* (Dunod, Paris, 1928), p. 193.

[38] Z. Che, T. N. Wong, and N.-T. Nguyen, Heat transfer in plug flow in cylindrical microcapillaries with constant surface heat flux, Int. J. Therm. Sci. **64**, 204 (2013).

[39] G. I. Taylor, Dispersion of soluble matter in solvent flowing slowly through a tube, Proc. R. Soc. London A **219**, 186 (1953).

[40] R. Aris, On the dispersion of a solute in a fluid flowing through a tube, Proc. R. Soc. London A **235**, 67 (1956).

[41] D. G. Levitt, Capillary-tissue exchange kinetics: An analysis of the Krogh cylinder model, J. Theor. Biol. **34**, 103 (1972).

[42] H. Brenner and K. Stewartson, Dispersion resulting from flow through spatially periodic porous media, Philos. Trans. R. Soc. A **297**, 81 (1980).

[43] J. Rubinstein and R. Mauri, Dispersion and convection in periodic porous media, SIAM J. Appl. Math. **46**, 1018 (1986).

[44] T. D. Tran Ngoc, J. Lewandowska, M. Vauclin, and H. Bertin, Two-scale modeling of solute dispersion in unsaturated double-porosity media: Homogenization and experimental validation, Int. J. Num. Anal. Methods Geomech. **35**, 1536 (2010).

[45] D. Picchi and P. Poesio, Dispersion of a passive scalar around a Taylor bubble, J. Fluid Mech. **951**, A22 (2022).

[46] R. P. Batycky, D. A. Edwards, and H. Brenner, Thermal Taylor dispersion in an insulated circular cylinder—I. Theory, Int. J. Heat Mass Transf. **36**, 4317 (1993).

[47] R. P. Batycky, D. A. Edwards, and H. Brenner, Thermal Taylor dispersion phenomena in nonadiabatic systems, Chem. Eng. Commun. **130**, 53 (1994).

[48] A. Liñán, P. Rajamanickam, A. D. Weiss, and A. L. Sánchez, Taylor-diffusion-controlled combustion in ducts, Combust. Theory Model. **24**, 1054 (2020).

[49] P. Botticini, D. Picchi, and P. Poesio, Forced convection in two-phase core-annular flows, J. Fluid Mech. **1011**, A41 (2025).

[50] J. G. Collier and J. R. Thome, *Convective Boiling and Condensation* (Oxford University Press, Oxford, UK, 1994).

[51] D. Picchi and I. Battiato, The impact of pore-scale flow regimes on upscaling of immiscible two-phase flow in porous media, Water Resour. Res. **54**, 6683 (2018).

[52] D. Picchi, A. Ullmann, and N. Brauner, Modeling of core-annular and plug flows of Newtonian/non-Newtonian shear-thinning fluids in pipes and capillary tubes, Int. J. Multiphase Flow **103**, 43 (2018).

[53] P.-G. de Gennes, F. Brochard-Wyart, and D. Quéré, *Capillarity and Wetting Phenomena: Drops, Bubbles, Pearls, Waves* (Springer, New York, NY, 2003).

[54] H. A. Stone, Interfaces: In fluid mechanics and across disciplines, J. Fluid Mech. **645**, 1 (2010).

[55] D. Picchi, A. Ullmann, N. Brauner, and P. Poesio, Motion of a confined bubble in a shear-thinning liquid, J. Fluid Mech. **918**, A7 (2021).

[56] M. Habibi Matin and S. Moghaddam, On the extension of Bretherton theory for thin liquid films formed around elongated bubbles, Phys. Fluids **33**, 123303 (2021).

[57] R. K. Shah and A. L. London, *Laminar Flow Forced Convection in Ducts* (Elsevier BV, Amsterdam, 1978).

[58] K. Chen, R. M. Cotta, C. P. Naveira-Cotta, and P. C. Pontes, Heat transfer analysis of compressible laminar flow in a parallel-plates channel via integral transforms, Int. Commun. Heat Mass Transfer **138**, 106368 (2022).

[59] P. J. Murphy, S. Alimohammadi, and S. M. O'Shaughnessy, Experimental investigation of dual jet flow past a heated surface: Effect of Reynolds number, Int. J. Heat Mass Transf. **218**, 124786 (2024).

[60] C. J. van Duijn, A. Mikelić, I. S. Pop, and C. Rosier, Effective dispersion equations for reactive flows with dominant Péclet and Damköhler numbers, in *Advances in Chemical Engineering*, Advances in Chemical Engineering, edited by G. B. Marin, D. West, and G. S. Yablonsky (Academic Press, San Diego, CA, 2008), Vol. 34, pp. 1–45.

[61] I. Battiato and D. M. Tartakovsky, Applicability regimes for macroscopic models of reactive transport in porous media, J. Contam. Hydrol. **120-121**, 18 (2011).

[62] B. Ling, A. M. Tartakovsky, and I. Battiato, Dispersion controlled by permeable surfaces: Surface properties and scaling, J. Fluid Mech. **801**, 13 (2016).
[63] R. Mauri, Heat and mass transport in random velocity fields with application to dispersion in porous media, J. Eng. Math. **29**, 77 (1995).
[64] J. Wloka, *Partial Differential Equations* (Cambridge University Press, Cambridge, UK, 1987).
[65] R. Mauri, Heat and mass transport in nonhomogeneous random velocity fields, Phys. Rev. E **68**, 066306 (2003).
[66] R. Mauri, Dispersion, convection, and reaction in porous media, Phys. Fluids **3**, 743 (1991).
[67] C. C. Mei and B. Vernescu, *Homogenization Methods for Multiscale Mechanics* (World Scientific, Singapore, 2010).
[68] A. Mikelić, V. Devigne, and C. J. van Duijn, Rigorous upscaling of the reactive flow through a pore, under dominant Péclet and Damköhler numbers, SIAM J. Math. Anal. **38**, 1262 (2006).
[69] M. Van Dyke, *Perturbation Methods in Fluid Mechanics*, Applied mathematics and mechanics, Vol. 8 (Academic Press, San Diego, CA, 1964).
[70] F. Feuillebois and A. Lasek, Computer aided application of the principle of least degeneracy, Z. Angew. Math. Phys. **28**, 1141 (1977).
[71] G. L. Richard, C. Ruyer-Quil, and J. P. Vila, A three-equation model for thin films down an inclined plane, J. Fluid Mech. **804**, 162 (2016).
[72] H. Brenner and D. A. Edwards, *Macrotransport Processes* (Butterworth-Heinemann, Oxford, UK, 1993).
[73] R. D. Skeel and M. Berzins, A method for the spatial discretization of parabolic equations in one space variable, SIAM J. Sci. Stat. Comput. **11**, 1 (1990).
[74] F. P. Incropera, *Fundamentals of Heat and Mass Transfer* (Wiley, New York, NY, 2007).
[75] S. Kjelstrup, D. Bedeaux, E. Johannessen, and J. Gross, *Non-Equilibrium Thermodynamics for Engineers*, 2nd ed. (World Scientific, Singapore, 2017).
[76] A. Bejan, *Heat Transfer* (John Wiley and Sons, New York, NY, 1993), p. 704.
[77] R. Gupta, D. F. Fletcher, and B. S. Haynes, CFD modelling of flow and heat transfer in the Taylor flow regime, Chem. Eng. Sci. **65**, 2094 (2010).
[78] E. Baird and K. Mohseni, Digitized heat transfer: A new paradigm for thermal management of compact micro systems, IEEE Trans. Compon. Packag. Technol. **31**, 143 (2008).
[79] A. Fershtman, L. Shemer, and D. Barnea, Instantaneous heat transfer rate around consecutive Taylor bubbles, Int. J. Heat Mass Transf. **95**, 865 (2016).
[80] Z. Che, T. N. Wong, and N.-T. Nguyen, Heat transfer enhancement by recirculating flow within liquid plugs in microchannels, Int. J. Heat Mass Transf. **55**, 1947 (2012).
[81] See Supplemental Material at http://link.aps.org/supplemental/10.1103/tf8n-pmmb for a movie illustrating the smoothing of the hotspot.
[82] P. Aussillous and D. Quéré, Quick deposition of a fluid on the wall of a tube, Phys. Fluids **12**, 2367 (2000).
[83] E. Klaseboer, R. Gupta, and R. Manica, An extended Bretherton model for long Taylor bubbles at moderate capillary numbers, Phys. Fluids **26**, 032107 (2014).
[84] A. de Ryck, The effect of weak inertia on the emptying of a tube, Phys. Fluids **14**, 2102 (2002).
[85] M. Magnini, A. Ferrari, J. R. Thome, and H. A. Stone, Undulations on the surface of elongated bubbles in confined gas-liquid flows, Phys. Rev. Fluids **2**, 084001 (2017).
[86] B. Dai, L. G. Leal, and A. Redondo, Disjoining pressure for nonuniform thin films, Phys. Rev. E **78**, 061602 (2008).
[87] H. Chen, E. Dong, J. Li, and H. A. Stone, Adhesion of moving droplets in microchannels, Appl. Phys. Lett. **103**, 131605 (2013).
[88] N. H. Hammoud, P. H. Trinh, P. D. Howell, and H. A. Stone, Influence of van der Waals forces on a bubble moving in a tube, Phys. Rev. Fluids **2**, 063601 (2017).
[89] D. Picchi, M. Berkani, G. Lavalle, and P. Poesio, Effect of the long-range van der Waals forces on the motion of an elongated bubble through a shear-thinning fluid, J. Non-Newtonian Fluid Mech. **349**, 105600 (2026).
[90] H. Schlichting, *Boundary Layer Theory* (Pergamon Press, London, UK, 1955).

[91] C. M. Bender and S. A. Orszag, *Advanced Mathematical Methods for Scientists and Engineers I: Asymptotic Methods and Perturbation Theory* (Springer, New York, NY, 1999).
[92] The MathWorks, Inc., *Partial Differential Equation Toolbox User's Guide* (The MathWorks, Inc., Natick, MA, 2025).
[93] Y. Z. Ma, Introduction to model upscaling, validation and history match, in *Quantitative Geosciences: Data Analytics, Geostatistics, Reservoir Characterization and Modeling* (Springer International Publishing, Cham, 2019), pp. 565–591.
[94] A. N. Asadolahi, R. Gupta, D. F. Fletcher, and B. S. Haynes, CFD approaches for the simulation of hydrodynamics and heat transfer in Taylor flow, Chem. Eng. Sci. **66**, 5575 (2011).
[95] F. Boso and I. Battiato, Homogenizability conditions for multicomponent reactive transport, Adv. Water Resour. **62**, 254 (2013).
[96] B. Ling, M. Oostrom, A. M. Tartakovsky, and I. Battiato, Hydrodynamic dispersion in thin channels with micro-structured porous walls, Phys. Fluids **30**, 076601 (2018).
[97] B. Ling, C. B. Rizzo, I. Battiato, and F. P. J. de Barros, Macroscale transport in channel-matrix systems via integral transforms, Phys. Rev. Fluids **6**, 044501 (2021).
[98] M. Magnini and M. A. Herrada, Two-dimensional global stability analysis of elongated bubbles moving in a horizontal tube, Phys. Rev. Fluids **10**, 053603 (2025).
[99] M. Magnini and J. R. Thome, An updated three-zone heat transfer model for slug flow boiling in microchannels, Int. J. Multiphase Flow **91**, 296 (2017).
[100] J. H. I. Lienhard and J. H. V. Lienhard, *A Heat Transfer Textbook*, 5th ed. (Phlogiston Press, Cambridge, MA, 2019).
[101] A. Vangeffelen, G. Buckinx, C. De Servi, M. R. Vetrano, and M. Baelmans, Nusselt number for steady periodically developed heat transfer in micro- and mini-channels with arrays of offset strip fins subject to a uniform heat flux, Int. J. Heat Mass Transf. **195**, 123145 (2022).
[102] M. Bhattacharya and T. Basak, On the definition of Nusselt number for convection within enclosures involving isothermal and non-isothermal walls, Int. Commun. Heat Mass Transfer **169**, 109416 (2025).
[103] W. M. Deen, *Analysis of Transport Phenomena* (Oxford University Press USA, New York, NY, 1998), p. 618.
[104] K. Fukagata, N. Kasagi, P. Ua-arayaporn, and T. Himeno, Numerical simulation of gas-liquid two-phase flow and convective heat transfer in a micro tube, Int. J. Heat Fluid Flow **28**, 72 (2007).
[105] Q. He, Y. Hasegawa, and N. Kasagi, Heat transfer modelling of gas-liquid slug flow without phase change in a micro tube, Int. J. Heat Fluid Flow **31**, 126 (2010).
[106] S. Kumari, N. Kumar, and R. Gupta, Flow and heat transfer in slug flow in microchannels: Effect of bubble volume, Int. J. Heat Mass Transf. **129**, 812 (2019).
[107] A. Mehdizadeh, S. A. Sherif, and W. E. Lear, Numerical simulation of thermofluid characteristics of two-phase slug flow in microchannels, Int. J. Heat Mass Transf. **54**, 3457 (2011).